Parallel use of pluripotent human stem cell lung and heart models provide new insights for treatment of SARS-CoV-2

Rajeev Rudraraju[1*], Matthew J Gartner[1*], Jessica A. Neil[1*], Elizabeth S. Stout[2*], Joseph Chen[3-5*], Elise J. Needham[6*], Michael See[2,7*], Charley Mackenzie-Kludas[1], Leo Yi Yang Lee[1], Mingyang Wang[1], Hayley Pointer[2], Kathy Karavendzas[2], Dad Abu-Bonsrah[2], Damien Drew[8], Yu Bo Yang Sun[3-5], Jia Ping Tan[3-5], Guizhi Sun[3-5], Abbas Salavaty[5,9], Natalie Charitakis[2,13], Hieu T. Nim[2,5,13], Peter D Currie[5,9], Wai-Hong Tham[8,10], Enzo Porrello[2,11,12,+ψ], Jose Polo[3,+ψ], Sean J. Humphrey[6,+ψ], Mirana Ramialison[2,5,13,+ψ], David A. Elliott[2,5,13,+ψ], Kanta Subbarao[1,14,+ψ]

[1]The Department of Microbiology and Immunology, The Peter Doherty Institute for Infection and Immunity, The University of Melbourne, Melbourne, 3000, Victoria, Australia.

[2]The Novo Nordisk Foundation Centre for Stem Cell Medicine (reNEW), Murdoch Children's Research Institute, Melbourne, 3052, Victoria, Australia.

[3]Department of Anatomy and Developmental Biology, Monash University, Clayton, Victoria, Australia.

[4]Development and Stem Cells Program, Monash Biomedicine Discovery Institute, Clayton, Victoria, Australia.

[5]Australian Regenerative Medicine Institute, Monash University, Clayton, Victoria, Australia.

[6]Charles Perkins Centre and School of Life and Environmental Sciences, Faculty of Science, The University of Sydney, Camperdown, NSW 2006 Australia.

[7] Monash Bioinformatics Platform, Monash University, Clayton, VIC 3800, Australia.

[8]Infection and Immunity Division, The Walter and Eliza Hall Institute of Medical Research, Victoria, Australia.

[9] EMBL Australia, Monash University, Clayton, VIC 3800, Australia.

[10]Department of Medical Biology, The University of Melbourne, Melbourne, VIC 3010, Australia.

[11]Melbourne Centre for Cardiovascular Genomics and Regenerative Medicine, The Royal Children's Hospital, Melbourne 3052, VIC, Australia.

[12]Department of Anatomy and Physiology, School of Biomedical Sciences, The University of Melbourne, Parkville, Australia.

[13]Department of Pediatrics, The Royal Children's Hospital, University of Melbourne Parkville, Victoria, 3052, Australia.

[14]The WHO Collaborating Centre for Reference and Research on Influenza, The Peter Doherty Institute for Infection and Immunity, Melbourne 3000, Victoria, Australia.

*These authors contributed equally.

[+, Ψ] Co-senior and co-corresponding authors.

The WHO Collaborating Centre for Reference and Research on Influenza, The Peter Doherty Institute for Infection and Immunity, Melbourne 3000, Victoria, Australia; The Department of Microbiology and Immunology, The Peter Doherty Institute for Infection and Immunity, The University of Melbourne, Melbourne, 3000, Victoria, Australia.

47 Contact: kanta.subbarao@influenzacentre.org

48

49 **Keywords:** SARS-CoV-2; COVID-19; human stem cell derived lung and heart models;
50 antiviral drugs

51 **One-sentence summary:** Rational treatment strategies for SARS-CoV-2 derived from
52 human PSC models

53

Abstract

SARS-CoV-2 primarily infects the respiratory tract, but pulmonary and cardiac complications occur in severe COVID-19. To elucidate molecular mechanisms in the lung and heart, we conducted paired experiments in human stem cell-derived lung alveolar type II (AT2) epithelial cell and cardiac cultures infected with SARS-CoV-2. With CRISPR-Cas9 mediated knock-out of ACE2, we demonstrated that angiotensin converting enzyme 2 (ACE2) was essential for SARS-CoV-2 infection of both cell types but further processing in lung cells required TMPRSS2 while cardiac cells required the endosomal pathway. Host responses were significantly different; transcriptome profiling and phosphoproteomics responses depended strongly on the cell type. We identified several antiviral compounds with distinct antiviral and toxicity profiles in lung AT2 and cardiac cells, highlighting the importance of using several relevant cell types for evaluation of antiviral drugs. Our data provide new insights into rational drug combinations for effective treatment of a virus that affects multiple organ systems.

Introduction

Coronavirus disease 19 (COVID-19) is primarily a respiratory disease. About 80% of infections are clinically mild or asymptomatic. Progression to severe illness is associated with lower respiratory tract involvement with pneumonia and acute respiratory distress syndrome (1, 2). Pulmonary fibrosis has been reported in survivors of COVID-19 (3).

In addition to pulmonary disease, cardiovascular, renal, digestive and neurological complications are reported (4). Cardiac complications include arrhythmias, thromboembolism, acute myocardial injury associated with elevated levels of cardiac troponin and electrocardiographic abnormalities (5, 6). Magnetic resonance imaging has shown cardiac involvement in up to 78% of recovered COVID-19 patients, and ongoing myocardial inflammation in 60% of patients (7, 8). Moreover, a meta-analysis of studies in COVID-19 patients found that myocardial injury was significantly associated with increased mortality (9). While cardiac damage during COVID-19 is predominantly thought to be due to an over-exuberant immune response, studies of autopsy tissue from patients who died from COVID-19 have detected viral RNA and Spike (S) antigen in the heart (10-12).

SARS-CoV-2 mediates infection by binding of the S protein to its receptor, angiotensin converting enzyme 2 (ACE2) on the host cell (13). The S protein is cleaved into two domains, S1 and S2 by host cell proteases, including furin (14). Following attachment, fusion with the cell membrane requires further proteolytic cleavage at the S2' site to activate the fusion peptide (15). This is mediated extracellularly by serine proteases

including Transmembrane protease, serine 2 (TMPRSS2) or in endosomes by Cathepsin L (15-17). Thus, ACE2 is a critical determinant of the tissue tropism of SARS-CoV-2, as are the presence of proteases and/or endosomal pathways for activation of the fusion activity of the S protein. ACE2 is expressed in many human tissues including the lungs, nose, cornea, heart, kidney, esophagus, gastrointestinal tract, liver, gallbladder placenta and testis, with high ACE2 expression observed in the nasal epithelium, lungs, ileum and heart (18-23). Tissue sites containing cells that co-express ACE2 and TMPRSS2 include the nose, lungs, kidney, gastrointestinal tract and the gallbladder (18, 22), while cells co-expressing ACE2 and Cathepsin L are found within the lung, heart and the gastrointestinal tract (22). Following entry, the virus interacts with the cellular machinery to complete its replication cycle and triggers a host cell response that can vary in different organs.

We sought to elucidate the molecular mechanisms of SARS-CoV-2 infection in lung and heart using human stem cell-derived lung and cardiac cells. Human pluripotent stem cells (hPSCs) including both human embryonic stem cells (hESCs) and induced pluripotent stem cells (hiPSCs) have been used to generate functional human cells, tissue and organoids to model human disease. We and others have generated stem cell-derived lung alveolar type II (AT2) epithelial cell and cardiac cultures that can be productively infected with SARS-CoV-2 (17, 24-26). We hypothesized that paired experiments in SARS-CoV-2 infected lung and cardiac cells would reveal important similarities and differences in viral and host factors that could inform treatment of COVID-19 and its complications. We used CRISPR-Cas9 mediated knock-out of ACE2 and demonstrated that ACE2 was essential for SARS-CoV-2 infection of both cell types. Small molecule

inhibitors revealed distinct mechanisms of SARS-CoV-2 entry. We identified differential cellular responses to SARS-CoV-2 infection by transcriptome profiling and phosphoproteomics and further demonstrated the utility of these stem cell-derived models for screening antiviral compounds for anti-SARS-CoV-2 activity. Our findings provide new insights into treatment strategies for COVID-19.

Results

SARS-CoV-2 productively infects human stem cell-derived lung AT2 and cardiac cultures

hESC and iPSC-derived cardiomyocyte (27, 28) and AT2 lung (29) cultures were generated to develop *in vitro* models of SARS-CoV-2 infection (Figure 1A). Lung AT2 cultures expressed high levels of lung development homeobox protein NKX2-1 and low levels of the type I alveolar cell marker Aquaporin-5 (AQP5) confirming the presence of low numbers of alveolar type I cells (Figure S1A). Gene expression profiling of the lung AT2 and cardiac cells demonstrated transcriptional profiles consistent with high levels of AT2 cells and cardiomyocytes, respectively (Figure S1B, C). For example, key cardiac genes such as those encoding myofilament proteins (*TNNT2*, *MYH7*, *MYL2* and *TTN*) and cardiomyocyte transcription factors (*HAND2*, *MEF2C* and *NKX2-5*) were expressed in cardiac cultures whilst the lung AT2 cultures expressed lung-specific development markers (*NKX2-1*, *SOX9* and *GATA6*) and signaling genes (*SHH* and *BMP4*).

To determine susceptibility to SARS-CoV-2 infection, lung AT2 and cardiac cells were inoculated with the ancestral strain of SARS-CoV-2. Vero cells were included in the experiment as a positive control for virus infection. As expected, SARS-CoV-2

137 productively infected Vero cells with virus titres and E gene copies, determined by
138 infectivity assay and qPCR respectively, peaking at 3 days post-infection (dpi) (Figure
139 1B). SARS-CoV-2 showed robust virus replication in lung AT2 cells, with virus titres and
140 E gene copies, peaking at 4 dpi (Figure 1B). Immunostaining for double stranded RNA
141 (dsRNA) showed evidence of SARS-CoV-2 replication at 3 dpi (Figure 1C). Cardiac cell
142 cultures differentiated from hESCs (*NKX2-5*$^{eGPF/w}$ (30)) were also susceptible to SARS-
143 CoV-2 infection with virus titres and E gene copies peaking slightly later than AT2 cells
144 between 4 and 6 dpi (Figure 1B). Cardiac cells generated from *ALPK3* knockout hESCs
145 that model hypertrophic cardiomyopathy (31), were similarly susceptible to SARS-CoV-2
146 infection with a peak in virus titres at 4 dpi (Figure S1D). Immunostaining showed SARS-
147 CoV-2 dsRNA in both cardiomyocyte and non-cardiomyocyte cells within the cardiac
148 monolayer cultures (Figure 1C). Furthermore, cardiac cultures infected with SARS-CoV-
149 2 stopped contracting at 4 dpi (Video S1). Overall, these data show that SARS-CoV-2
150 replicates efficiently in cardiac and lung AT2 cells derived *in vitro* from hPSCs, consistent
151 with published reports (17, 24).

152 To determine whether cardiac and lung AT2 cells are susceptible to infection by
153 SARS-CoV-2 variants, virus titres and E gene copies were assessed following infection
154 with Alpha, Beta, Gamma, Delta and Omicron (BA.1 and BA.2) variants. Although all
155 variants were able to infect the lung AT2 cells, a modest difference was observed
156 following Delta infection in lung AT2 cells at 1 and 3 dpi (Figure 1D, S1E) but titres were
157 comparable to all other variants by 5 dpi. In cardiac cells, a slightly lower virus titer was
158 observed following infection with the Alpha variant at 3 dpi (Figure 1D). However, this was
159 not observed for E gene copies where WT levels were higher than other variants on 1

and 3 dpi (Figure S1E). In lung AT2 cells, the Omicron subvariants showed similar titres to the WT virus, although BA.1 showed a modest reduction in virus titres and E gene copies compared to BA.2 (Figure 1E, S1F). In cardiac cells, the BA.1 and BA.2 variants showed significantly lower virus titres compared to the WT virus at 2-5dpi (Figure 1E). However, this difference in replication was not observed for E gene copies (Figure S1F). These data confirm that hPSCs derived *in vitro* models can be used to study all variants and that SARS-CoV-2 variants infect cardiac and lung cells efficiently.

SARS-CoV-2 infection in lung AT2 and cardiac cells is dependent on ACE2

ACE2 is the functional receptor for sarbecoviruses, the SARS coronavirus family. To confirm that ACE2 is required for SARS-CoV-2 infection in cardiac and lung AT2 cells, we generated two *ACE2* knockout (KO) hPSC lines (H9 and MCRIi010-A) engineered via CRISPR/Cas9 to remove the first coding exon of ACE2 (Figure S2A and B). ACE2 protein and *ACE2* transcript expression was not detected in either lung AT2 or cardiac cultures differentiated from the *ACE2* knockout line (Figure S2C and D). Flow cytometric analysis confirmed that the genetically modified cells maintained their expression of pluripotency markers and showed similar differentiation capacity (Figure S2E and F). Furthermore, immunofluorescence staining in ACE2 KO cardiac or lung AT2 cells showed that ACE2 expression was undetectable (Figure S2H).

Following confirmation that ACE2 was knocked out in H9 and MCRIi010-A lines, cardiomyocyte and AT2 differentiation protocols were performed. The ACE2 KO cardiac or lung AT2 cells could not be productively infected with SARS-CoV-2, as shown by the inability to recover infectious virus and absence of dsRNA staining (Figure 2A, S2G-

S2H). For independent confirmation of the role of ACE2, we used a combination of two previously described α-ACE2 antibodies at doses between 2-40 µg/mL (23). In cardiac cultures, 2 µg/mL of α-ACE2 antibodies was sufficient to completely block SARS-CoV-2 infection (Figure 2B). In contrast, treatment with the α-ACE2 antibody cocktail blocked infection in a concentration-dependent fashion in lung AT2 cells (Figure 2B). Overall, our data demonstrate that SARS-CoV-2 infection in lung AT2 and cardiac cells is dependent on ACE2 for virus entry.

SARS-CoV-2 utilizes differential entry mechanisms in lung AT2 and cardiac cells

Following attachment to the host cell receptor, coronaviruses require proteolytic activation of the spike protein to mediate fusion of the viral and host cell membranes. SARS-CoV-2 can be activated for fusion at the cell membrane through transmembrane protease, serine 2 (TMPRSS2) mediated cleavage of the (S2') site or through endocytosis, where endosomal acidification triggers Cathepsin L (CSTL)-activated fusion between the viral and endolysosomal membranes. While lung AT2 cells had high expression of *TMPRSS2*, cardiac cells did not express *TMPRSS2* (Figure S3A, B). In contrast, both lung AT2 and cardiac cells expressed *CSTL* at high levels (Figure S3A, B) suggesting that SARS-CoV-2 may enter cardiac cells via the endocytosis pathway.

To determine the mechanism of entry, cells were infected in the presence of the TMPRSS2 inhibitor Camostat mesylate or the Cathepsin B/L inhibitor CA-074 Me. Camostat treatment (100, 10 and 1 µM) led to a significant reduction in virus titer and genome copies in lung AT2 but not in cardiac cells (Figure 2C and S3C) showing that infection in lung AT2 cells requires TMPRSS2 cleavage. In contrast, 25 µM of CA-074 Me

led to a significant reduction in virus titer and genome copies in cardiac but not in lung AT2 cells (Figure 2C and S3C), confirming that the viral entry in cardiac cells requires the endosomal pathway. Thus, consistent with the gene expression data, SARS-CoV-2 utilizes distinct entry pathways in lung AT2 and cardiac cells.

Antiviral compounds show differential activity in lung and cardiac cells compared to traditional cell lines

To determine whether SARS-CoV-2 antiviral drugs show similar activity in lung AT2 and cardiac cells, we investigated two sets of small molecules: (a) drugs that are approved for treatment of COVID-19 including Remdesivir and NHC (β-D-N4-hydroxycytidine), the prodrug of Molnupiravir and (b) drugs that were reported to show antiviral activity *in vitro* but are still under clinical investigation or were not found to be effective in clinical trials including favipiravir, tizoxanide (the active form of the antiparasitic agent nitazoxanide), and chloroquine.

Remdesivir and NHC significantly inhibited viral replication in both cardiac and lung AT2 cells (Figure 2D, E). In Vero cells, remdesivir inhibited virus replication at a concentration of 10 μM while in lung AT2 cells, the drug completely inhibited virus replication at concentrations as low as 2.5 μM (IC_{50} = 0.55 μM) and antiviral activity in cardiac cells was far more potent, with complete inhibition of viral replication at 0.08 μM (IC_{50}=0.016 μM) (Figure 2D). Similarly, NHC was more effective in inhibiting virus replication in cardiac cells compared to lung AT2 and Vero cells, with complete virus inhibition observed at concentrations as low as 5 μM (IC_{50}=0.42 μM) (Figure 2E) while viral replication was inhibited in Vero and lung AT2 cells with similar dose-response

kinetics (IC_{50}=2.4 μM and 3.54 μM, respectively) (Figure 2E). In terms of toxicity, reduced viability of both lung AT2 and cardiac cells was observed with remdesivir concentrations above 5 μM but not in Vero cells (Figure S4A). NHC was noticeably less toxic than remdesivir in all three cell types, with toxicity observed at the concentration of 40 μM in cardiac and lung AT2 cells (Figure S4B). These results highlight the variability in both antiviral efficacy and cytotoxicity in different cell types and emphasize the relevance of using human stem-cell derived models or human cells over Vero cells for assessment of antiviral drugs for COVID-19.

Favipiravir, piperaquine and tizoxanide showed no antiviral activity against SARS-CoV-2 in cardiac, lung AT2 and Vero cells up to a concentration of 10 μM (Figure S4C). Of these three compounds, tizoxanide was toxic in Vero cells but not in cardiac or lung AT2 cells (Figure S4C). Chloroquine was not toxic in any of the cell types and inhibited SARS-CoV-2 virus replication in cardiac cells (at 10 μM) but not in lung AT2 or Vero cells (Figure S4C), consistent with our observation that SARS-CoV-2 entry in cardiac cells utilizes the endosomal pathway. Chloroquine also inhibited virus replication in the *ALPK3* KO cardiomyopathy model (Figure S4C). Together, these data indicate that the activity of antiviral drugs differs between lung AT2 and cardiac cells compared to conventionally used Vero cells.

SARS-CoV-2 induces different transcriptional responses in lung AT2 and cardiac cells

Based on our observation of distinct entry pathways and antiviral activity between lung AT2 and cardiac cells, we hypothesized that they would show diverse responses to SARS-CoV-2 infection. RNA-sequencing (RNA-seq) was performed on cell lysates from

hESC-derived lung AT2 and cardiac cells infected with SARS-CoV-2 at 1 and 3 dpi. A principal component analysis (PCA) plot separated the tissue types and demonstrated a progressive separation between mock-infected and virus-infected cells particularly by 3 dpi (Figure 3A). At 1 dpi, no differentially expressed genes (DEGs) were observed in lung AT2 cells, and only 5 in cardiac cells (data not shown). However, at 3 dpi, 1154 and 992 DEGs were obtained for cardiac and lung AT2 cells, respectively, with specific lung and cardiac specific DEGs. As shown in Figure 3B, of the DEGs between the 2 cell-types, 202 were overlapping (intersect), 952 genes were differentially expressed in the cardiac cells only (cardiac unique) and 790 genes were differentially expressed in the lung AT2 cells only (lung unique). Additionally, we found that SARS-CoV-2 infection did not change the expression profile of lung development genes in lung AT2 cells and cardiac development genes in cardiac cells at 1 and 3 dpi (Figure S1B and C).

WikiPathway enrichment analysis of DEG subsets identified that the biological processes impacted by SARS-CoV-2 infection in both lung AT2 and cardiac cells (i.e. intersect subset), included Electron Transport Chain (OXPHOS system in mitochondria) (WP111), Host-pathogen interaction of human coronaviruses – Interferon (IFN) induction (WP4880) and Type I and II IFN signaling pathways (Figure 3C; Figure S5A, B). However, only 3 genes in the “Intersect” subset involved Type II IFN signaling, indicating only a relatively small response. In contrast, the "cardiac unique" gene subset, included an overall upregulation of genes in Type III interferon signaling (WP2113) and downregulation of genes in the Striated Muscle Contraction Pathway (WP383), consistent with the cessation of contractility of SARS-CoV-2 infected cultures (Video S1). In the “lung unique” subset, we observed an overall downregulation of genes in Amino Acid

metabolism (WP3925) and upregulation of genes in Ethanol metabolism resulting in production of reactive oxygen species (ROS) by CYP2E1 (WP4269) (Figure 3C).

Key differences in the transcriptional responses to SARS-CoV-2 infection between lung AT2 and cardiac cells were the IFN pathways that were activated (Figure 3C, D). By 3 dpi, genes from the Type I, II and III IFN pathways (*IFNB1*, *CXCL10*, *PRKCD*, *IFNL1*, *IFNL2* and *IFNL3*) were upregulated in cardiac but not lung AT2 cells. Concordant with the observed increase in transcription by RNASeq, cytokine analysis showed a significant induction of IL-6, IP-10, IFN-λ1, IFN-λ2/3 and IFN-β in infected cardiac cells, but not lung AT2 cells, at 3 dpi compared to mock-infected controls (Figure 3E). Furthermore, qPCR showed induction of *IFITM3*, *IFN-β*, *STAT1* and *STAT2* in infected cardiac cells, and not lung AT2 cells, compared to mock-infected cells at 3 dpi (Figure S5C). Network analysis of the GO term response to interferon gamma showed multiple genes within the network were upregulated in infected cardiac but not lung AT2 cells (Figure S5D). Taken together, SARS-CoV-2 infection in cardiac induces robust Type I, II and III IFN responses but not in lung AT2 cells.

SARS-CoV-2 activates druggable kinases in lung AT2 and cardiac cells

We measured the phosphoproteome to determine the signaling responses of lung AT2 and cardiac cells to SARS-CoV-2 infection. Cells were either mock-infected or infected with SARS-CoV-2 and sampled at 0-, 18-, 24- and 72- hours post inoculation (Figure 4A). Only viral phosphorylation sites were analyzed at the 72 hours timepoint. By employing recent advances in phosphoproteomics technologies (32), we quantified >32,000 phosphopeptides in at least three samples (Figure 4B). The phosphoproteomes

clustered primarily by tissue origin in PCA (PC1), emphasizing the cell-type specific nature of signaling (Figure 4C). Time since infection was the second largest factor affecting clustering by PCA (on PC2), due to the long time-points studied. For this reason, a 'mock' condition was sampled at every timepoint, enabling identification of infection-driven signaling. SARS-CoV-2 infection extensively regulated cellular signaling, with at least 250 phosphopeptides regulated at each timepoint (Figure 4D). Regulation of the phosphoproteome was most extensive in cardiac cells at 18 hours post-infection (>900 phosphopeptides altered). Remarkably only 12 and 15 phosphopeptides were commonly regulated between the cardiac and lung AT2 cells at the 18- and 24- hour timepoints, respectively (Figure 4E). This low overlap of regulation was also observed at the transcriptional level and indicates that the response to SARS-CoV-2 is highly contextual and depends strongly on the cell type or tissue of origin.

To corroborate this, we sought to identify the molecular drivers of the SARS-CoV-2 infection response, by integrating RNA-seq and phosphoproteomics datasets using ExIR (https://influential.erc.monash.edu/). This analysis revealed that the top 3 drivers of SARS-CoV-2 infection response in cardiac cells (*SP110*, *STAT1* and *DTX3L*) were activators of the interferon response (Fig. 4F, G). In contrast, no strong interferon pathway activators were identified in the top drivers of the infection response in lung AT2 cells, confirming the specificity of the interferon response only in cardiac cells. To determine the cellular context of SARS-CoV2-regulated signaling, we tested for enrichment of cellular components (Figure S6A). Endosomal components almost uniquely enriched in the SARS-CoV2 response of cardiac cells, and not lung cells (Figure 4H, Figure S6A). This mirrors the pattern of viral entry occurring via endocytosis in cardiac cells.

We next explored the upstream regulators of the SARS-CoV-2 signaling response to identify molecular targets important for SARS-CoV-2 replication. By mapping reported kinase-substrate relationships to our phosphoproteomics data, we found that 37 kinases had substrates that were enriched for regulated phosphosites (Figure S6B, Figure 4I). We hypothesized that kinases with substrates enriched in up-regulated phosphorylation sites had increased activity in the SARS-CoV-2 response, and *vice versa* for kinases with down-regulated sites. The unique signaling responses of cardiac and lung cells was also evident at the kinase level, as of the 37 kinases enriched in at least one condition, 6 were significantly enriched in the same direction in both cell types. For kinases such as Protein Kinase C (PKC), some isoforms had opposite cell type-specific patterns of regulation. Of the PKC isoforms, PKCD had substrates enriched in upregulated sites in the lung cells, while PKCT was enriched in the cardiac cells (Figure 4I). This could suggest some convergence in signaling outcomes despite differing proteins being employed. However, the gold standard PKC substrate MARCKS S170 was uniquely upregulated in cardiac cells (Figure 4J).

Since SARS-CoV-2 proteins can also be phosphorylated by host kinases, we also searched our phosphoproteomics data specifically for phosphorylation of SARS-CoV-2 viral proteins. We measured 32 sites on 5 viral proteins (ORF1a, S, M, N and ORF9b (Table S1). This list includes S206 on the nucleocapsid protein, which has been reported as an SRSF Protein Kinase 1 (SRPK1) substrate (Figure 4K, (33)).

Differential antiviral activity of candidate compounds in cardiac and lung AT2 cells

Based on the different transcriptional and phosphoproteomics data observed in lung and cardiac cells, we hypothesized that selected compounds would inhibit SARS-CoV-2 replication differentially. We interrogated our molecular datasets to predict new and alternative druggable targets. We selected 9 pathways that were differentially phosphorylated in SARS-CoV-2 infected lung AT2 and cardiac cells and identified 15 compounds that could inhibit the kinases critical for these pathways. These kinases (and their inhibitors) included: LIM domain kinase (R-10015), Checkpoint Kinases 2 (CCT241533 HCL), SRSF Protein Kinase 1 (Alectinib, SPHINX31), Cyclin-dependent Kinases (CDKs) (CCT251545, SNS-032, Palbociclib hydrochloride, Flavopiridol, Dinaciclib, Abemaciclib, Samuraciclib hydrochloride hydrate, Trilaciclib hydrochloride), Glycogen synthase kinase-3 (AZD1080) and protein kinase C (Bisindolylmaleimide I). We also tested an inhibitor of the TGFβ pathway using an inhibitor of the TGFβ type II receptor (GW788388). We screened the compounds at concentrations of 1, 10 and 50 μM for antiviral activity (data not shown) based on which we eliminated three compounds that targeted CDKs based on their strong toxicity in cardiac cells and lack of activity in lung cells (Flavopiridol, Dinaciclib, Samuraciclib hydrochloride hydrate). SNS-032 was analyzed further although it was toxic in cardiac cells because it showed promising antiviral activity in lung AT2 cells. We evaluated the remaining 12 compounds across a dose range from 0.04 to 30 μM for antiviral activity and cell cytotoxicity in both cardiac (H9 and NKX2-5)) and lung AT2 (H9) cells. Antiviral activity (% inhibition compared to the Vehicle control) was tested against nanoluciferase (nLuc)-expressing SARS-CoV-2 and an ancestral strain of SARS-CoV-2 (VIC01) by measuring luciferase expression and E gene copies, respectively. NHC was used as a positive control in all the antiviral assays

While the CDK8 inhibitor CCT251545 was ineffective in limiting SARS-CoV-2 replication (Figure S7), CDK4/6 inhibitors Abemacicilib, Palbociclib and Trilacicilib restricted virus replication in at least one cell type (Figure 5A). Abemaciclib and Palbociclib inhibited virus replication in both cell types, while Trilaciclib hydrochloride inhibited in cardiac cells with variable inhibition in the lung AT2 cells (Figure 5A). CDK2/7/9 inhibitor SNS-032 showed significant antiviral activity with minimal cytotoxicity in lung AT2 cells but was cytotoxic in cardiac cells (Figure 5A). In the lung AT2 cells, CHK inhibitor CCT241533HCl and PKC inhibitor Bisindolylmaleimide 1 showed some antiviral activity at the highest concentrations tested but were cytotoxic at these concentrations (Figure 5B, C). In cardiac cells, antiviral activity was observed with the CHK and PKC inhibitors at concentrations that were not cytotoxic (Figure 5B, C).

Alectinib and SPHINX31, which inhibit SRPK1, inhibited viral replication in both lung AT2 and cardiac cells (Figure 5D). Our data suggest that while SRPK1 inhibitors can restrict viral replication in both cell types, greater inhibition was observed in lung AT2 cells. Similar activity of these antiviral drugs was observed in H9-derived cardiac cells (Figure S7A). Drugs that targeted LIM domain kinase (R-10015) and TGFβ type II receptor (GW788388) showed no activity in either cell type (Figure S7B). The GSK-3 inhibitor, AZD1080, showed no antiviral activity in H9-derived lung AT2 and cardiac cells (Figure S7). However, it did show antiviral activity in NKX2-5 cardiac cells against VIC01 but not the nLuc virus suggesting that removal of ORF7a may affect drug sensitivity (Figure S7,(2)). Overall, these data show that inhibition of kinases with small molecular inhibitors can abrogate SARS-CoV-2 replication with differing effectiveness in cardiac and lung cells.

Discussion

Our data from parallel evaluation of SARS-CoV-2 infection in stem cell-derived cardiac and lung AT2 cells provide valuable insights into virus-host interactions in tissues that are significantly affected in COVID-19, with implications for rational design of therapeutic interventions. The key take-home messages from our study are that virus entry, cellular response, antiviral activity and cytotoxicity differ in SARS-CoV-2 infected human cardiac and lung AT2 cells and both differ from what is seen in African monkey kidney derived Vero cells that are widely used for SARS-CoV-2 research. Virus entry in both human cell types is dependent on ACE2 but further processing of the S protein is mediated through TMPRSS2 in lung AT2 cells, while infection of cardiac cells is achieved through the endosomal pathway and Cathepsin L. Host responses are significantly different, with a strong interferon response following infection in cardiac cells but not in lung AT2 cells. Phosphoproteomic analysis identified activation of different pathways in cardiac and lung AT2 cells. Parallel evaluation of antiviral activity and cytotoxicity of drugs in cardiac and lung AT2 cells reveals several points to consider in COVID-19 therapy, including the use of drug combinations to target both membrane protease and endosomal entry pathways, drugs that target SRPK1 and CDKs, and the importance of using relevant human stem-cell derived models in place of immortalized cell lines such as Vero cells for assessment of antiviral drugs.

Early reports characterizing SARS-CoV-2 demonstrated the requirement of ACE2 for virus entry (34). Our RNA-seq and qPCR analysis of lung and cardiac cells demonstrated high ACE2 expression in lung AT2 cells and low expression in cardiac cells. Immunofluorescence analysis of ACE2 expression in lung AT2 cells showed that only a

small proportion of cells expressed ACE2, consistent with previous reports showing heterogeneous ACE2 expression in iPSC-derived and adult AT2 cells (24, 35). Despite low ACE2 expression in cardiac cells, virus replication was robust in this system achieving titres of more than 100,000 $TCID_{50}$/mL by days four and six post-infection. Furthermore, SARS-CoV-2 infection of ACE2 KO lung AT2 and cardiac cells completely abolished virus growth, demonstrating that ACE2 is required for infection of these cells, consistent with previous reports using similar models (17, 36-38). Moreover, we showed that SARS-CoV-2 infection was blocked with a combination of anti-ACE2 antibodies. Anti-ACE2 antibodies at a low dose did not completely block infection in AT2 cells but did in cardiac cultures, likely reflecting the difference in ACE2 expression between the cell types. Overall, we show that ACE2 expression is required for SARS-CoV-2 infection in stem-cell derived lung AT2 and cardiac cells.

To investigate the protease requirements for entry into stem-cell derived AT2 and cardiac cells, we performed entry inhibition assays with the TMPRSS2 inhibitor Camostat mesylate and the Cathepsin B/L inhibitor CA-074 Me (39). Camostat inhibited SARS-CoV-2 infection in AT2 cells, suggesting that TMPRSS2 is required for SARS-CoV-2 infection of AT2 cells, consistent with previous reports (24, 40). In contrast, CA-074 Me blocked SARS-CoV-2 infection in cardiac cells, demonstrating that Cathepsin L cleavage through endosomal entry is required for infection of cardiac cells, consistent with previous studies (17, 37, 38). The ability of SARS-CoV-2 to enter cells through different pathways may explain why clinical trials of Camostat mesylate in COVID-19 hospitalized patients and hydroxychloroquine alone did not result in clinical benefit (41). Our data suggest that a combination of drugs that target both pathways may be more effective *in vivo* and

emphasize the importance of antiviral testing in several relevant tissue types. Ou *et al* reported that 10uM Camostat in combination with 10uM Hydroxychloroquine reduced virus replication compared to Camostat alone in Calu3 cells (42) and a clinical trial of Hydroxychloroquine in combination with Camostat is registered at clinicaltrials.gov (NCT04355052).

We found a robust interferon response in cardiac cells, which was not observed in lung AT2 cells. Induction of interferon in infected cardiac cell cultures has been previously reported using bulk RNA-seq (36, 38). However, Perez-Bermejo *et al* reported that single cell RNA-seq of infected iPSC-derived cardiomyocytes showed an induction of proinflammatory cytokines, but not type I or III interferons (17). A potential explanation for the discrepancy between our findings and those of Perez-Bermejo *et al* is that the additional cells present in our cultures (fibroblasts, smooth muscle cells and endothelial cells, (43)) or bystander cardiomyocytes are responsible for inducing robust interferon responses.

In contrast to cardiac cells, SARS-CoV-2 infection did not induce an interferon response in lung AT2 cells, consistent with another study of stem-cell derived AT2 models (44). The difference in host response to infection between cardiac cells and lung AT2 cells may be explained by the viral entry pathways. SARS-CoV-2 replication leads to detection of double stranded RNA (dsRNA) replication intermediates by Melanoma-differentiation-associated gene 5 (MDA5) and induction of a robust interferon response through Mitochondrial Antiviral Signaling Protein (MAVS) signaling (44, 45). Several studies have identified SARS-CoV-2 proteins (nsp1, nsp5, nsp6, nsp13, nsp15, ORF6 and ORF7b) that inhibit MAVS-induced Type I and III interferon responses (46-48). This

453 mechanism of interferon antagonism likely explains the lack of interferon induction seen
454 in lung AT2 cells following SARS-CoV-2 infection. In contrast, endosomal entry of SARS-
455 CoV-2 in cardiac cells may explain the robust induction of interferon. Endosomes contain
456 toll-like receptors (TLRs) including TLR3 and TLR7/8 that sense dsRNA and ssRNA, with
457 only TLR3 detectable in cardiomyocytes (49). Furthermore, defects in TLR3 have been
458 associated with disease severity in patients (50), suggesting TLR3 may play an important
459 role in inducing interferon responses.

460 Although COVID-19 vaccines are highly effective in preventing severe illness and
461 death, antiviral compounds are required for the treatment of COVID-19, particularly with
462 the emergence of variant viruses and reduced effectiveness of vaccines in preventing
463 symptomatic illness caused by variants of concern. To date, only a handful of drugs
464 including Remdesivir, Molnupiravir and Paxlovid have been approved for use in
465 hospitalized COVID-19 patients and additional drugs are needed. In this study, we
466 established two cellular models relevant to COVID-19 disease that are scalable and
467 amenable to high throughput screening. We used this system to screen drugs that
468 advanced to clinical trials based on *in vitro* activity against SARS-CoV-2. We noted poor
469 antiviral activity of Remdesivir in Vero cells compared to stem cell-derived lung AT2 cells
470 and cardiac cells. These data are consistent with a previous report showing Remdesivir
471 is metabolized inefficiently in Vero cells (51) and suggests that Vero cells are not optimal
472 for screening antiviral compounds against SARS-CoV-2.

473 Based on results from phosphoproteomics analysis, we screened several kinase
474 inhibitors for their ability to inhibit viral replication in lung AT2 and cardiac cells. Out of 12
475 compounds we evaluated, three had activity in both AT2 and cardiac cells (SPHINX31,

476 Alectinib, Abemaciclib), one had activity in AT2 cells only (SNS-032), four had activity in
477 cardiac cells only (CCT241533, Palbociclib, Trilaciclib, Bisindolylmaleimide I) and the
478 remaining were ineffective. We observed that several CDK inhibitors were toxic at the
479 concentrations tested, particularly in cardiac cells. Of note SNS-032 showed strong
480 antiviral activity in lung AT2 cells but induced cardiac cell death; medicinal chemistry
481 approaches could be explored to limit the toxicity for cardiac cells. Effectiveness of
482 SRPK1 and CDK inhibitors against SARS-CoV-2 has been reported previously in Vero,
483 Calu-3, A549-ACE2 cells and primary lung cells (33, 52). However, this is the first study
484 to show potential toxicity of CDK inhibitors in cardiac cells. Although we observed antiviral
485 activity in both cell types, SRPK1 inhibitors were effective at lower concentrations in lung
486 AT2 compared to cardiac cells. Overall, we have identified several antiviral compounds
487 with distinct effectiveness and toxicity profiles in lung AT2 and cardiac cells, highlighting
488 the importance of using several cell types for evaluation of antiviral effectiveness.

489 In summary, with paired experiments in human stem cell derived tissue surrogates
490 of organs that are affected in severe COVID-19, we have demonstrated important
491 commonalities and several key differences in virus-host interactions in lung and cardiac
492 cells. While the value of using human lung organoids, A549 and Calu-3 cells for evaluation
493 of antiviral drugs has been recognized, our work highlights the importance of evaluation
494 in additional relevant cells (lung and heart) for the evaluation of antiviral activity and
495 cytotoxicity of drugs that are considered for treatment of COVID-19. This parallel
496 evaluation in two cell types offers novel insights into rational design of therapeutic
497 interventions.

498

Acknowledgements

This work was supported by The Medical Research Future Fund (MRF9200007; K.S., E.R.P., J.M.P., D.A.E.) and the Victorian State Government (Victorian State Government (DJPR/COVID-19; KS, MR, ERP, J.P., D.A.E.) and COVID-19 Victorian Consortium (KS). E.R.P., M.R., D.A.E. are supported by The Novo Nordisk Foundation Center for Stem Cell Medicine (Grant NNF21CC0073729), The Stafford Fox Medical Research Foundation and The Royal Children's Hospital Foundation. Fellowship support provided by National Health and Medical Research Council of Australia (E.R.P. and KS). MCRI is supported by the Victorian Government's Operational Infrastructure Support Program. The Melbourne WHO Collaborating Centre for Reference and Research on Influenza is supported by the Australian Government Department of Health.

Author Contributions

Conceptualization and design: E.P, J.P, S.J.H, M.R, D.E and K.S. Data acquisition: R.R, M.J.G, J.A.N, E.S.S, J.S, E.J.D, M.S, C.M-K, L.Y.Y.L, M.W, H.P, K.K and D.A-B. Data analysis and Interpretation: R.R, M.J.G, J.A.N, E.S.S, J.S, E.D, M.S, A.S, N.C, H.T.N and P.D.C. Reagent production: D.D and W-H.T. Manuscript preparation: R.R, M.J.G, J.A.N and K.S. Manuscript edits and proofing: E.S.S, J.S, E.J.D, M.S, E.P, J.P, S.H, M.R and D.E. All authors critically reviewed and approved the final version of the manuscript.

Materials and Methods

Cells. African green monkey kidney epithelial (Vero cells, ATCC Cat. CCL-81), Vero hSLAM (Merck, Car. 04091501), Calu-3 (ATCC, Cat. HTB-55) and VeroE6-TMPRSS2 (CellBank Australia, Cat. JCRB1819) cells were cultured at 37°C and 5% CO_2. Vero cell media: Minimum Essential Media (MEM) (Media Preparation Unit, Peter Doherty Institute) supplemented with 5% Fetal Bovine Serum (FBS, Bovogen, Cat. SFBS), 50U/mL Penicillin and 50µg/mL Streptomycin (PenStrep, Thermo Fisher Scientific, Cat. 15070-063), 2mM GlutaMAX (Thermo Fisher Scientific, Cat. 35050061) and 15 mM HEPES (Thermo Fisher Scientific, Cat. 15630130). Vero hSLAM cell media: MEM supplemented with 7% FBS, PenStrep, 2mM GlutaMAX, 15 mM HEPES and 0.4 mg/mL G418 Sulfate (Gibco, Cat. 10131027). Calu-3 cell media: MEM containing L-glutamine and sodium bicarbonate (Sigma, Cat. M4655) supplemented with 10% FBS, PenStrep, 1x non-essential amino acids (Gibco, Cat. 11140050) and sodium pyruvate (Fisher Scientific, Cat. BP356-100). VeroE6-TMPRSS2 cell media: Dulbecco's Minimum Essential Media (DMEM) (Media Preparation Unit, Peter Doherty Institute) supplemented with 10% FBS, PenStrep, 2mM GlutaMAX and 1 mg/mL G418 Sulfate.

Viruses. SARS-CoV-2 viruses hCoV-19/Australia/VIC01/2020 (VIC01, GISAID ID: EPI_ISL_406844), hCoV-19/Australia/VIC17991/2020 (Alpha variant, GISAID ID: EPI_ISL_779606), hCoV-19/Australia/QLD1520/2020 (Beta variant, GISAID ID: EPI_ISL_968081), hCoV-19/Australia/VIC18440/2021 (Delta variant, GISAID ID: EPI_ISL_1913206), hCoV-19/Australia/NSW-RPAH-1933/2021 (Omicron BA.1 variant, GISAID ID: EPI_ISL_6814922) and hCoV-19/Australia/VIC35864/2022 (Omicron BA.2

variant, GISAID ID: EPI_ISL_8955536) were a kind gift obtained from the Victorian Infectious Diseases Reference Laboratory (VIDRL). hCoV-19/Japan/TY7-503/2021 (Gamma variant, GISAID ID: EPI_ISL_877769, NR-54982) was obtained through BEI Resources, NIAID, NIH, contributed by National Institute of Infectious Diseases. icSARS-CoV-2-nLuc virus was a kind gift from Prof Ralph S. Baric from the Department of Microbiology and Immunology, University of North Carolina at Chapel Hill, Chapel Hill, NC, USA (2). SARS-CoV-2 VIC01 was propagated in Vero and Vero hSLAM cells in Vero infection medium (serum-free MEM in the presence of 1µg/mL TPCK-Trypsin (Cat. LS003740)). SARS-CoV-2 Alpha, Beta, Gamma and Delta variants were propagated in Vero hSLAM cells in infection medium (serum-free MEM with 1µg/mL TPCK-Trypsin). SARS-CoV-2 Omicron BA.1 and BA.2 variants were passaged in Calu3 cells in infection media (MEM containing 2% FBS). Virus stocks were stored at -80°C and titered as described below.

Virus Titration. Virus titrations were performed in 96 well plates with confluent Vero and VeroE6-TMPRSS2 monolayers. Cells were washed with plain MEM and replaced with 180 µL of serum-free media containing 1µg/mL TPCK-Trypsin. Each sample was titrated in quadruplicate by adding 20µL of supernatant to first well and performing 10-fold serial dilutions. Cells were incubated at 37°C and assessed microscopically for SARS-CoV-2-induced cytopathic effect (CPE) on day 4. Virus titres are expressed as mean $\log_{10}TCID_{50}$/mL.

566 **Viral RNA extraction and RT-PCR.** RNA was extracted as per the manufacturer's
567 recommendation using QiaCube HT (Qiagen) and QiaAmp 96 Virus QiaCube HT kit
568 (Qiagen, Cat. 57731). RT-PCR reaction was setup using SensiFast Probe No-ROX One-
569 Step Kit (Bioline, Cat. BIO-76005) using the following primers/probes: E_Sarbeco_F1: 5'-
570 ACAGGTACGTTAATAGTTAATAGCGT-3', E_Sarbeco_R2: 5'-
571 ATATTGCAGCAGTACGCACACA-3'), E_Sarbeco_P1_FAM: 5'-
572 ACACTAGCCATCCTTACTGCGCTTCG-3'. Serial 10-fold dilutions of plasmid encoding
573 the viral E gene were used to generate a standard curve for calculating the virus genome
574 copies in the samples.
575
576 **Lung alveolar type 2 cell differentiation.** Induced pluripotent H9 (female) stem cells
577 were seeded onto flasks coated with Matrigel (Corning, Cat. 354230) in Essential 8
578 medium (Thermo Fisher Scientific, Cat. A1517001). After 48 h, medium was changed
579 daily with RPMI 1640 (Thermo Fisher Scientific, Cat. 21870084) supplemented with B-27
580 (Gibco, Cat. 17504044), 100ng/mL Activin A (Peprotech, Cat. 120-14P), 1μM CHIR99021
581 (Sigma-Aldrich, Cat. SML1046), PenStrep for 3 days. On days 4-8, medium was changed
582 daily with DMEM/F12 media (Thermo Fisher Scientific, Cat. 105650) supplemented with
583 N2 (Gibco, Cat. 17502048), B27, 0.05mg/mL Ascorbic Acid (Sigma-Aldrich, Cat.
584 A92902), 0.4mM Monothioglycerol (Sigma-Aldrich, Cat. M6145), 2μM Dorsomorphin
585 (Stemcell Technologies, Cat.72102), SB431542 (Miltenyi Biotec, Cat. 130-106-543) and
586 PenStrep. On days 9-12, medium was changed daily with DMEM/F12-based medium with
587 B27, 0.05mg/mL Ascorbic Acid, 0.4mM Monothioglycerol, 20ng/mL BMP4 (Peprotech,
588 Cat. 120-05ET), 0.5μM Retinoic Acid (ATRA) (Sigma-Aldrich, Cat. R2625), 3μM

589 CHIR99021, PenStrep. Day 12 and onwards, medium was changed every other day with
590 DMEM/F12 supplemented with B27, 0.05mg/ml Ascorbic Acid, 0.4mM Monothioglycerol,
591 10ng/mL FGF10 (Stemcell Technologies, Cat. 78037), 10ng/mL FGF7 (Peprotech, Cat.
592 10019), 3μM CHIR99021, 50nM Dexamethasone (Sigma-Aldrich, Cat. D4902), 0.1mM 8-
593 Bromoadenosine 3′,5′-cyclic monophosphate (8-Br-cAMP) (Sigma-Aldrich, Cat.
594 B5386), 0.1mM 3-Isobutyl-1-methylxanthine (IBMX) (Sigma-Aldrich, Cat. I5879) and
595 PenStrep. Cultures were embedded onto Matrigel on day 18 in 12-well plates. On day 30,
596 organoids were dissociated in TrypLE (Thermo Fisher Scientific, Cat. 12604013) for 3
597 mins before re-embedding in Matrigel. Lung organoids were maintained for experiments
598 between passage 2-8 prior to dissociation with TrypLE and seeding onto Geltrex (Gibco,
599 Cat. A1413201) -coated plates supplemented with Y-27632 (Selleck Chemicals, Cat,
600 S1049) at the initial seeding step. Cells were maintained for a further 7-10 days in 2D
601 culture until infection at 70%+ confluency.
602
603 **Cardiac Cell Differentiation**. The human embryonic stem cell lines HES3 *NKX2-5*$^{eGFP/w}$
604 and H9 (both female), and human induced pluripotent stem cell line MCRIi010-A (male),
605 were used for viral infection studies in 2D monolayer cultures. Each stem cell line and
606 their derivatives were cultured as outlined previously (30). Cardiomyocytes cultures were
607 differentiated as previously described and cryopreserved at day 10 following
608 differentiation (27). Cells were subsequently thawed in basal differentiation media
609 containing RPMI 1640 (Thermo Fisher Scientific, Cat. 21870), 2% B27 without vitamin A
610 (Thermo Fisher Scientific, Cat. 12587), 1% Glutamax (Thermo Fisher Scientific, Cat.
611 35050), 0.5% PenStrep (Thermo Fisher Scientific, Cat. 15070) and 10 μM Y-27632 for 24

hours at 37ºC. Cells were then maintained in basal differentiation medium for an additional 2 days. To enrich for cardiomyocytes, cells were cultured for 2 days in lactate purification media as described previously (53). The cells were maintained in maturation media, as described previously (43), from day 15 to day 23 post differentiation prior to viral infection.

CRISPR/Cas9 ACE2 KO line generation. For CRISPR/Cas9 knock-out of *ACE2*, synthetic oligonucleotides containing sgRNAs (5' sgRNA 5'- CACCGTCTAGGGAAAGTCATTCAG-3' and 5'- AAACCTGAATGACTTTCCCTAGAC-3' and 3' sgRNA 2 5'- CACCGCAGTAATCTAATCTTTAAG-3' and 5'- AAACCTTAAAGATTAGATTACTGC-3' targeting the first coding exon of *ACE2* were generated with overhangs for BbsI digestion and subsequent cloning into pX458 (Addgene, Cat. 48138) as described previously. Cells were harvested with TrypLE, and transfections were performed using the Neon Transfection System (Thermo Fisher Scientific). Electroporation was performed in a 100 µL tip using the following conditions: 1050 V, 30 ms, 2 pulses. Following electroporation, cells were transferred to flasks containing mitotically inactivated MEFs and HES or iPSC media (without PenStrep) with 5 µM Y-27632, which was omitted in subsequent media changes. Cells transiently expressing EGFP were single cell sorted, colonies were grown for 2 weeks and screened via PCR.

Clone characterization: karyotyping, pluripotency, and differentiation. Genomic integrity of ACE2 KO lines was assessed using the Illumina Infinium GSA-24 v2.0 and

635 was performed by the Victorian Clinical Genetics Service, Royal Children's Hospital
636 (Melbourne). Pluripotency was examined via expression of EPCAM-BV421 (Biolegend,
637 Cat. 324220), CD9-FITC (BD Biosciences, Cat. 555371) and SSEA4-PE/Cy7 (Biolegend,
638 Cat. 330420) expression using flow cytometry. IgG-BV421, IgG-FITC and IgG-PE/Cy7
639 (Biolegend, Cat. 400158 and BD Biosciences Cat. 555748, 400126) were used for isotype
640 controls. Cardiac cultures generated from the WT and ACE2 KO lines were then
641 assessed using cardiomyocyte specific markers, cardiac troponin T and α-Actinin
642 (Abcam, Cat. AB45932, A7811) to demonstrate comparable levels of cardiomyocyte
643 differentiation. AF488 and AF647 (Thermo Fisher Scientific Cat. A11034, A21236) were
644 used for detection on the LSR Fortessa X-20 Flow cytometer (BD Biosciences).
645
646 **Quantitative PCR.** Total RNA was extracted using Trizol reagent (Thermo Fisher
647 Scientific, Cat. 15596026) following the manufacturer's protocol or using the RNeasy Mini
648 Kit (Qiagen, Cat. 74106). cDNA synthesis was conducted using the SuperScript™ VILO™
649 Master Mix (Thermo Fisher Scientific, Cat. 11755050) according to the manufacturer's
650 instructions. Quantitative real-time PCR (qPCR) was performed with either TaqMan Fast
651 Advanced Master Mix, TaqMan™ Gene Expression Master Mix or PowerUp™ SYBR™
652 Green Master Mix (Thermo Fisher Scientific, Cat. 4444557, 4369510 or A25777
653 respectively). The Taqman probes (Thermo Fisher Scientific, Cat. 4453320) are listed in
654 Table S3. Green are as follows: *ACE2* 5'-TTAACCACGAAGCCGAAGAC-3' and 5'-
655 TACATTTGGGCAAGTGTGGA-3'; 5'-CCTGGCTGAAAGACCAGAAC-3' and 5'-
656 GCAACAGATGATCGGAACAG-3'; and 5'- GGTTGGCATTGTCATCCTG-3' and 5'
657 GGAGGTCTGAACATCATCAGTG-3'. Glyceraldehyde-3-phosphate dehydrogenase

(*GAPDH*) (5' TGCACCACCAACTGCTTAGC-3' and 5' GGCATGGACTGTGGTCATGAG -3') was used as a housekeeping gene for normalization.

Western blot analysis. hESC and iPSC-derived cardiac and lung AT2 cells were lysed in high salt RIPA buffer (RIPA+0.5M NaCl) with added Protease inhibitor (Sigma-Aldrich, Cat. 5056489001) and phosSTOP (Roche, Cat. 4906845001). Lung AT2 lysates were made using Laemmli sample buffer (Bio-Rad, Cat: #1610737EDU). Total protein concentration was measured by BCA assay (Thermo Fisher Scientific, Cat. 23227). 20 µg of samples were loaded into a 4–20% Mini-PROTEAN pre-cast gel (Bio-Rad, Cat: 4561093) and ran at 70 V for 30 min, followed by ~70 min at 120 V. Protein was transferred to PVDF membrane and blocked in 5% skim milk in Tris-buffered saline contain Tween-20 (TBST) for 1 h. The membrane was incubated with primary antibodies against ACE2 (Abcam, Cat. 15348, 1:1000 in 5% skim milk overnight at 4ºC) and GAPDH as a loading control (Fitzgerald Industries International, Cat. 10R-2932, 1:3000 in 5% skim milk/TBST for 1 h at room temperature (RT)). HRP-linked antibodies (Bio-Rad, Cat. 1706516 and Cell Signaling Technology, Cat. 7074S) were then used at 1:3000 in skim milk/TBST for 1 h at RT. Blots were imaged on a GE Amersham Imager 680 following addition of ECL substrate (Bio-rad, Cat. 170-5060).

Virus growth in lung AT2, cardiac and Vero cells. Infection of human ESC and iPSC-derived cells and Vero cells was performed in 24 well tissue culture plates. Vero cells were washed with MEM prior to infection. Media was removed and replaced with 10^4 $TCID_{50}$ of SARS-CoV-2 in 100ul and incubated for 1 h at RT. The inoculum was removed, cells washed twice with cell-specific media and refed with media. The second wash was

harvested for day 0 sampling. Vero cells were cultured in serum-free media containing 1µg/mL TPCK-Trypsin. Supernatants were collected each day and media was replenished. Harvested supernatants were stored at -80°C to determine infectious virus titres and E gene copies.

Immunofluorescence. Cells were fixed with 4% PFA and blocked with blocking buffer (1% horse serum and 0.1% Triton X-100 in phosphate-buffered saline (PBS)) and stained with primary antibodies (cTNT: Thermo Fisher Scientific, Cat. MA1-16687, 1:200; dsRNA: Australian Bioresearch, Cat, ab01299-2.0, 1:200; SP-C: Santa Cruz Biotechnology, Cat. sc-518029,1:100; AQP5: Santa Cruz Biotechnology, Cat. sc-514022, 1:100; NKX2.1: Abcam, Cat. ab76013, 1:100) overnight at 4ºC. Cells were washed with PBS and stained with secondary antibodies from Invitrogen (Mouse IgG2a AF594 Cat. A21135, Mouse IgG1 AF647 Cat. A21240, Rabbit IgG AF555 Cat. A21428, Mouse IgG2b AF488 Cat. A21141, Mouse IgG2a AF555 Cat. A21127, Rabbit IgG AF647 Cat. 21244) and Hoechst 33342 (Life Technologies) at 1:1000 in blocking buffer for 1-2 hours at RT. For ACE2 staining, cells were blocked with 10% normal goat serum (Thermo Fisher Scientific, Cat. PCN5000) in PBSTT (PBS with 0.1% Triton-X and 0.1% Tween). Primary ACE2 antibodies (WCSL141, (23)) and cTNT antibodies were left to incubate overnight at 4ºC in 5% goat serum in PBSTT before being washed in PBS and probed with secondary antibodies (Jackson Immuno, Cat. 709-116-098 at 1:100 and Hoescht at 1:200).

SARS-CoV-2 entry inhibition. Lung AT2 and cardiac cells seeded into 24 well plates were treated with 100µL of α-ACE2 antibodies (WCSL141 and WCSL148, (23)), human

IgG isotype control, Camostat Mesylate (Sigma Aldrich, Cat. SML0057) or DMSO for 1 h at 37°C. Subsequently, 10^4 $TCID_{50}$ of SARS-CoV-2 was added to cells and incubated for 1 h at 37°C. Virus inoculum was removed, and cells were washed with plain MEM twice before replacement with the 500µL cell-specific culture media. For CA-074 Me inhibition, cells seeded into 24 well plates were treated with 200µL of CA-074 Me (Selleck Chemicals, Cat. S7420) for 2 h at 37°C. Subsequently, 10^4 $TCID_{50}$ of SARS-CoV-2 was added to cells and incubated for 1 h at 37°C. Supernatant samples were obtained daily, and the media was replaced with drug-containing media until day 3. Infectious virus titres and E gene copies were determined as detailed above.

Antiviral testing. Compounds remdesivir (MedChemExpress, Cat. HY104077), NHC (β-D-N4-hydroxycytidine, MedChemExpress, Cat. HY125033), favipiravir (Toyama Chemicals Co. Ltd, Japan, T705), tizoxanide (Romark Laboratories, Tampa, FL) chloroquine (Sigma Aldrich, Cat. C6628) and piperaquine (Sigma Aldrich, Cat. C7874) were tested in lung AT2, cardiac and Vero cells in 24 well tissue culture plates. Vero cells were washed with MEM prior to addition of 100µL of cell type-specific media containing diluted compounds. The vehicle controls were prepared to contain the same amount of vehicle (DMSO or water) as the 10µM of compound. One hour after addition of diluted compound, 100µL of media containing 10^4 $TCID_{50}$ of SARS-CoV-2 (and 1µg/ml TPCK-Trypsin for Vero cells) was added and incubated for an additional hour at RT. The inoculum was removed and replaced with 500µL of cell-specific media containing diluted compounds. At 3 dpi, supernatants were harvested and stored at -80°C. Infectious virus titres and E gene copies were determined as detailed above.

Kinase inhibitor compounds (Table S2) were tested in lung AT2 and cardiac cells seeded in 96 well culture plates. Cells were incubated with 200µL of cell-specific media containing 30µM to 0.04µM of compound for 2 h at 37℃. DMSO was maintained consistently to a final concentration of 0.1%. After 2 h, 10^4 $TCID_{50}$ of icSARS-CoV-2-nLuc or VIC01 was added to each well (20uL total) and cells were incubated at 37°C for 2 days. Cell supernatant from VIC01-infected cells was collected for measurement of E-gene copies as detailed above. For nLuc virus detection, cells were lysed with Passive Lysis Buffer (Promega, Cat. E1941) and luciferase expression measured using Nano-Glo Luciferase Assay System (Promega, Cat. N1130) as per the manufacturer's instructions. Luminescence was measured on FLUOstar Omega (BMG Labtech).

Antiviral toxicity testing. All compounds were tested in lung AT2, cardiac and Vero cells in 96 well tissue culture plates. Vero cells were washed with 200µL of MEM. After removal of media, 100µL of cell type-specific media containing diluted compound was added. At day 2 (Kinase inhibitors) or day 3 (other compounds), cell viability was measuring using the CellTiter-Glo®2.0 cell viability kit (Promega, Cat. G9241) as per manufacturer's recommendations. Luminescence was measured on FLUOstar Omega (BMG Labtech).

RNA Sequencing Analysis. Human stem cell-derived cardiac and lung cells grown in 24 well tissue culture plates were infected with 10^4 $TCID_{50}$ of SARS-CoV-2. At 0-, 1- and 3-days post-infection, supernatant was removed, and the cell monolayer was lysed with

500µL of TRIzol reagent (Life Technologies Australia PTY LTD, Cat. 15596018). RNA was extracted following the manufacturer's protocol.

RNA Sequencing data were demultiplexed using a modified version of the Sabre demultiplexer to produce a single fastq file per sample. Fastq files were processed using the RNAsik pipeline [https://doi.org/10.21105/joss.00583]. Reads were aligned to EnsEMBL GRCh38 (54) using the STAR aligner (55) and duplicates were marked with Picard ["http://broadinstitute.github.io/picard/"]. Aligned reads were quantified to gene level counts using featureCounts (56). Next, differential gene expression analysis was performed in Degust [https://doi.org/10.5281/zenodo.3501067] using the EdgeR QL method (57) to produce sets of differentially expressed genes for Cardiac and Lung conditions, respectively. The sets of differentially expressed genes were processed for pathway enrichment using Metascape (58) with default parameters except that only the WikiPathways ontology was used. Figures were generated using R [4] and tidyverse [https://doi.org/10.21105/joss.01686] packages. RNA-seq data have been submitted to the NCBI GEO database (GSE212003).

LEGENDplex. Cytokine/chemokine concentrations in supernatant from mock and SARS-CoV-2 infected lung AT2 and cardiac cells were analyzed using the LEGENDplex human anti-virus response panel (Biolegend, Cat. 740390) following the manufacturer's instructions. Samples were run on a BD FACSCanto II and analyzed using LEGENDplex™ Data Analysis Software Suite (v8).

Phosphoproteomics. Human cardiac and lung AT2 cells grown in 6 well tissue culture plates inoculated with mock or SARS-CoV-2 were harvested at 0-, 18- and 24- hours post-inoculation for phosphoproteomic analysis. Briefly, media was removed and replaced with 500µL of respective media containing $5x10^4$ $TCID_{50}$ of SARS-CoV-2. Mock wells received 500µL of media alone. After infection for 1 h, inoculum was removed and replaced with 2000µL of respective media. At selected timepoints post-infection, wells were washed four times with 5ml of ice-cold TBS. After TBS removal, cells were lysed with 100µL of lysis buffer (6M Guanidinium chloride, 100mM Tris pH 8.5), inactivated at 95°C for 5 minutes and frozen at -80°C. Upon thawing, lysates were sonicated with a tip-probe sonicator (50% output power, 30 seconds), and an aliquot was diluted 1:5 in 8M Urea to determine protein concentration by BCA assay. Protein (250 µg) was diluted in SDC buffer, reduced and alkylated at 45°C for 5 min by the addition of 10 mM Tris (2-carboxyethyl) phosphine (TCEP)/40 mM 2-Chloroacetamide (CAA) pH 8, and digested by the addition of 1:100 Lys-C and Trypsin overnight at 37°C with agitation (1,500 rpm). After digestion phosphopeptides were enriched in parallel using the high-sensitivity EasyPhos workflow as previously described (32). Eluted phosphopeptides were dried in a SpeedVac concentrator (Eppendorf) and resuspended in MS loading buffer (0.3% TFA/2% acetonitrile) prior to LC-MS/MS measurement.

Phosphopeptides were loaded onto a 55 cm column fabricated in-house, from 75µM inner diameter fused silica packed with 1.9µM C18 ReproSil particles (Dr. Maisch GmBH), and column temperature was maintained at 60°C using a Sonation column oven. A Dionex U3000 RSLC Nano HPLC system (Thermo Fisher Scientific) was interfaced with a Q Exactive HF X benchtop Orbitrap mass spectrometer using a NanoSpray Flex ion source

(Thermo Fisher Scientific). Peptides were separated with a binary buffer system of 0.1% (v/v) formic acid (buffer A) and 80% (v/v) acetonitrile / 0.1% (v/v) formic acid (buffer B) at a flow rate of 400nL/min, and separated with a gradient of 3-19% buffer B over 40 min, followed by 19-41% buffer B over 20 min, resulting in a gradient time of 60 min. Peptides were analyzed in Data Independent Acquisition (DIA) mode, with one full scan (350-1,400 m/z; R = 120,000 at 200 m/z) at a target of 3e6 ions, followed by 48 DIA MS2 scans using HCD (target 3e6 ions; max. IT 22 ms; isolation window 14.0 m/z; NCE 25%, window overlap 1m/z), detected in the Orbitrap mass analyzer (R = 15,000 at 200 m/z). RAW MS data was processed using Spectronaut v15.4.210913.50606, with searches performed using the directDIA method against the Human and SARS-CoV2 UniProt databases (January 2021 and October 2021 releases respectively). Default “BGS Phospho PTM Workflow” settings were used, with a linear model used for PTM Consolidation, Cross Run Normalization enabled, and a localization Probability Cutoff of 0.5. Data filtering mode was set to ‘Qvalue’.

Phosphoproteomes were log transformed and median normalized. Ratios of SARS-CoV-2 to the median mock values were taken for each timepoint in each cell type. Regulated phosphopeptides were identified with a one-way ANOVA for each cell type separately. P-values were adjusted for multiple hypothesis testing with the q-value R package. Dunnett’s post hoc tests were performed to determine the timepoint at which the regulation occurred, with the 0-hour timepoint as the control condition. Enrichment of regulated phosphosites was determined by ranking phosphosites by their Log2FC and performing a modified weighted gene set enrichment analysis, implemented in the R

816 package ksea. Cellular component annotation was obtained from GO and reported
817 kinase-substrate relationships were obtained from PhosphoSitePlus.
818
819 **Integration of RNA-seq and phosphoproteomics.** To systematically identify and
820 prioritize the drivers of the molecular response to SARS-CoV-2 infection, based on the
821 combination of transcriptomics and phospho-proteomics data, we run the ExIR model
822 separately on heart and lung datasets using the R package influential (https://cran.r-
823 project.org/package=influential). ExIR is a versatile one-stop model for the extraction and
824 prioritization of candidates from high-throughput data. In particular, we used the following
825 three input data for running the ExIR model: 1) entire transcriptomic dataset as the
826 experimental data, 2) table of differentially expressed genes, and 3) the list of differentially
827 phosphorylated proteins at 72-hour time-point as the desired list of features. In this way,
828 the ExIR model is built based on the differentially phosphorylated proteins in the context
829 of the transcriptomic data. Lastly, the top five drivers prioritized by ExIR were visualized
830 separately for lung and heart dataset.
831
832 **Statistical analysis.** All data were plotted and analyzed using GraphPad Prism 9. Log_{10}
833 virus titres and E gene copies were analyzed using either a student's T-test or two-way
834 ANOVA with Tukey's or Dunnett's multiple comparisons test as appropriate. *, $p<0.05$; **,
835 $p<0.01$; ***, $p<0.001$ and ****, $p<0.0001$. Dotted lines indicate the lower limit of detection
836 of the assay unless indicated otherwise. Data are representative of at least two
837 independent experiments showing mean (±SD) unless indicated overwise. Antiviral
838 activity and cytotoxicity data for the kinase inhibitors (Fig 5 and S7) was analyzed by

calculating percent inhibition/viability relative to vehicle control. Curve fitting was performed using non-linear regression (four parameters – variable slope) with data constrained between 0 and 100.

References

1. Chen PZ, Bobrovitz N, Premji ZA, Koopmans M, Fisman DN, and Gu FX. SARS-CoV-2 shedding dynamics across the respiratory tract, sex, and disease severity for adult and pediatric COVID-19. *Elife.* 2021;10.
2. Hou YJ, Okuda K, Edwards CE, Martinez DR, Asakura T, Dinnon KH, 3rd, et al. SARS-CoV-2 Reverse Genetics Reveals a Variable Infection Gradient in the Respiratory Tract. *Cell.* 2020;182(2):429-46 e14.
3. Huang C, Huang L, Wang Y, Li X, Ren L, Gu X, et al. 6-month consequences of COVID-19 in patients discharged from hospital: a cohort study. *Lancet.* 2021;397(10270):220-32.
4. Nalbandian A, Sehgal K, Gupta A, Madhavan MV, McGroder C, Stevens JS, et al. Post-acute COVID-19 syndrome. *Nat Med.* 2021;27(4):601-15.
5. Lazzerini PE, Laghi-Pasini F, Boutjdir M, and Capecchi PL. Inflammatory cytokines and cardiac arrhythmias: the lesson from COVID-19. *Nat Rev Immunol.* 2022;22(5):270-2.
6. Shi S, Qin M, Shen B, Cai Y, Liu T, Yang F, et al. Association of Cardiac Injury With Mortality in Hospitalized Patients With COVID-19 in Wuhan, China. *JAMA Cardiol.* 2020;5(7):802-10.
7. Puntmann VO, Carerj ML, Wieters I, Fahim M, Arendt C, Hoffmann J, et al. Outcomes of Cardiovascular Magnetic Resonance Imaging in Patients Recently Recovered From Coronavirus Disease 2019 (COVID-19). *JAMA Cardiol.* 2020;5(11):1265-73.

884 8. Goyal P, Choi JJ, Pinheiro LC, Schenck EJ, Chen R, Jabri A, et al. Clinical
885 Characteristics of Covid-19 in New York City. *N Engl J Med.* 2020;382(24):2372-
886 4.
887 9. Shao MJ, Shang LX, Luo JY, Shi J, Zhao Y, Li XM, et al. Myocardial injury is
888 associated with higher mortality in patients with coronavirus disease 2019: a meta-
889 analysis. *J Geriatr Cardiol.* 2020;17(4):224-8.
890 10. Deinhardt-Emmer S, Wittschieber D, Sanft J, Kleemann S, Elschner S, Haupt KF,
891 et al. Early postmortem mapping of SARS-CoV-2 RNA in patients with COVID-19
892 and the correlation with tissue damage. *Elife.* 2021;10.
893 11. Wang XM, Mannan R, Xiao L, Abdulfatah E, Qiao Y, Farver C, et al.
894 Characterization of SARS-CoV-2 and host entry factors distribution in a COVID-19
895 autopsy series. *Commun Med (Lond).* 2021;1:24.
896 12. Schneider J, Pease D, Navaratnarajah C, Halfmann P, Clemens D, Ye D, et al.
897 SARS-CoV-2 direct cardiac damage through spike-mediated cardiomyocyte
898 fusion. *Research Square.* 2020.
899 13. Zhou P, Yang XL, Wang XG, Hu B, Zhang L, Zhang W, et al. A pneumonia
900 outbreak associated with a new coronavirus of probable bat origin. *Nature.*
901 2020;579(7798):270-3.
902 14. Shang J, Wan Y, Luo C, Ye G, Geng Q, Auerbach A, et al. Cell entry mechanisms
903 of SARS-CoV-2. *Proc Natl Acad Sci U S A.* 2020;117(21):11727-34.
904 15. Hoffmann M, Kleine-Weber H, Schroeder S, Kruger N, Herrler T, Erichsen S, et al.
905 SARS-CoV-2 Cell Entry Depends on ACE2 and TMPRSS2 and Is Blocked by a
906 Clinically Proven Protease Inhibitor. *Cell.* 2020;181(2):271-80 e8.

16. Ou X, Liu Y, Lei X, Li P, Mi D, Ren L, et al. Characterization of spike glycoprotein of SARS-CoV-2 on virus entry and its immune cross-reactivity with SARS-CoV. *Nat Commun.* 2020;11(1):1620.

17. Perez-Bermejo JA, Kang S, Rockwood SJ, Simoneau CR, Joy DA, Silva AC, et al. SARS-CoV-2 infection of human iPSC-derived cardiac cells reflects cytopathic features in hearts of patients with COVID-19. *Sci Transl Med.* 2021;13(590).

18. Sungnak W, Huang N, Becavin C, Berg M, Queen R, Litvinukova M, et al. SARS-CoV-2 entry factors are highly expressed in nasal epithelial cells together with innate immune genes. *Nat Med.* 2020;26(5):681-7.

19. Qi F, Qian S, Zhang S, and Zhang Z. Single cell RNA sequencing of 13 human tissues identify cell types and receptors of human coronaviruses. *Biochem Biophys Res Commun.* 2020;526(1):135-40.

20. Zou X, Chen K, Zou J, Han P, Hao J, and Han Z. Single-cell RNA-seq data analysis on the receptor ACE2 expression reveals the potential risk of different human organs vulnerable to 2019-nCoV infection. *Front Med.* 2020;14(2):185-92.

21. Hamming I, Timens W, Bulthuis ML, Lely AT, Navis G, and van Goor H. Tissue distribution of ACE2 protein, the functional receptor for SARS coronavirus. A first step in understanding SARS pathogenesis. *J Pathol.* 2004;203(2):631-7.

22. Muus C, Luecken MD, Eraslan G, Sikkema L, Waghray A, Heimberg G, et al. Single-cell meta-analysis of SARS-CoV-2 entry genes across tissues and demographics. *Nat Med.* 2021;27(3):546-59.

928 23. Chen J, Neil J, Tan J, Rudraraju R, Mohenska M, Sun Y, et al. An iTSC-derived
929 placental model of SARS-CoV-2 infection reveals ACE2-dependent susceptibility
930 in syncytiotrophoblasts. *bioRxiv.* 2021:2021.10.27.465224.
931 24. Huang J, Hume AJ, Abo KM, Werder RB, Villacorta-Martin C, Alysandratos KD, et
932 al. SARS-CoV-2 Infection of Pluripotent Stem Cell-Derived Human Lung Alveolar
933 Type 2 Cells Elicits a Rapid Epithelial-Intrinsic Inflammatory Response. *Cell Stem*
934 *Cell.* 2020;27(6):962-73 e7.
935 25. Sharma A, Garcia G, Jr., Wang Y, Plummer JT, Morizono K, Arumugaswami V, et
936 al. Human iPSC-Derived Cardiomyocytes Are Susceptible to SARS-CoV-2
937 Infection. *Cell Rep Med.* 2020;1(4):100052.
938 26. Williams TL, Colzani MT, Macrae RGC, Robinson EL, Bloor S, Greenwood EJD,
939 et al. Human embryonic stem cell-derived cardiomyocyte platform screens
940 inhibitors of SARS-CoV-2 infection. *Commun Biol.* 2021;4(1):926.
941 27. Anderson DJ, Kaplan DI, Bell KM, Koutsis K, Haynes JM, Mills RJ, et al. NKX2-5
942 regulates human cardiomyogenesis via a HEY2 dependent transcriptional
943 network. *Nat Commun.* 2018;9(1):1373.
944 28. Lopes LR, Garcia-Hernandez S, Lorenzini M, Futema M, Chumakova O,
945 Zateyshchikov D, et al. Alpha-protein kinase 3 (ALPK3) truncating variants are a
946 cause of autosomal dominant hypertrophic cardiomyopathy. *Eur Heart J.*
947 2021;42(32):3063-73.
948 29. Jacob A, Morley M, Hawkins F, McCauley KB, Jean JC, Heins H, et al.
949 Differentiation of Human Pluripotent Stem Cells into Functional Lung Alveolar
950 Epithelial Cells. *Cell Stem Cell.* 2017;21(4):472-88 e10.

30. Elliott DA, Braam SR, Koutsis K, Ng ES, Jenny R, Lagerqvist EL, et al. NKX2-5(eGFP/w) hESCs for isolation of human cardiac progenitors and cardiomyocytes. *Nat Methods.* 2011;8(12):1037-40.

31. Phelan DG, Anderson DJ, Howden SE, Wong RC, Hickey PF, Pope K, et al. ALPK3-deficient cardiomyocytes generated from patient-derived induced pluripotent stem cells and mutant human embryonic stem cells display abnormal calcium handling and establish that ALPK3 deficiency underlies familial cardiomyopathy. *Eur Heart J.* 2016;37(33):2586-90.

32. Humphrey SJ, Karayel O, James DE, and Mann M. High-throughput and high-sensitivity phosphoproteomics with the EasyPhos platform. *Nat Protoc.* 2018;13(9):1897-916.

33. Yaron TM, Heaton BE, Levy TM, Johnson JL, Jordan TX, Cohen BM, et al. The FDA-approved drug Alectinib compromises SARS-CoV-2 nucleocapsid phosphorylation and inhibits viral infection in vitro. *bioRxiv.* 2020.

34. Zhou P, Yang XL, Wang XG, Hu B, Zhang L, Zhang W, et al. Addendum: A pneumonia outbreak associated with a new coronavirus of probable bat origin. *Nature.* 2020;588(7836):E6.

35. Ziegler CGK, Allon SJ, Nyquist SK, Mbano IM, Miao VN, Tzouanas CN, et al. SARS-CoV-2 Receptor ACE2 Is an Interferon-Stimulated Gene in Human Airway Epithelial Cells and Is Detected in Specific Cell Subsets across Tissues. *Cell.* 2020;181(5):1016-35 e19.

36. Marchiano S, Hsiang TY, Khanna A, Higashi T, Whitmore LS, Bargehr J, et al. SARS-CoV-2 Infects Human Pluripotent Stem Cell-Derived Cardiomyocytes,

Impairing Electrical and Mechanical Function. *Stem Cell Reports.* 2021;16(3):478-92.

37. Bojkova D, Wagner JUG, Shumliakivska M, Aslan GS, Saleem U, Hansen A, et al. SARS-CoV-2 infects and induces cytotoxic effects in human cardiomyocytes. *Cardiovasc Res.* 2020;116(14):2207-15.

38. Bailey AL, Dmytrenko O, Greenberg L, Bredemeyer AL, Ma P, Liu J, et al. SARS-CoV-2 Infects Human Engineered Heart Tissues and Models COVID-19 Myocarditis. *JACC Basic Transl Sci.* 2021;6(4):331-45.

39. Montaser M, Lalmanach G, and Mach L. CA-074, but not its methyl ester CA-074Me, is a selective inhibitor of cathepsin B within living cells. *Biol Chem.* 2002;383(7-8):1305-8.

40. Tiwari SK, Wang S, Smith D, Carlin AF, and Rana TM. Revealing Tissue-Specific SARS-CoV-2 Infection and Host Responses using Human Stem Cell-Derived Lung and Cerebral Organoids. *Stem Cell Reports.* 2021;16(3):437-45.

41. Gunst JD, Staerke NB, Pahus MH, Kristensen LH, Bodilsen J, Lohse N, et al. Efficacy of the TMPRSS2 inhibitor camostat mesilate in patients hospitalized with Covid-19-a double-blind randomized controlled trial. *EClinicalMedicine.* 2021;35:100849.

42. Ou T, Mou H, Zhang L, Ojha A, Choe H, and Farzan M. Hydroxychloroquine-mediated inhibition of SARS-CoV-2 entry is attenuated by TMPRSS2. *PLoS Pathog.* 2021;17(1):e1009212.

43. Mills RJ, Titmarsh DM, Koenig X, Parker BL, Ryall JG, Quaife-Ryan GA, et al. Functional screening in human cardiac organoids reveals a metabolic mechanism

997 for cardiomyocyte cell cycle arrest. *Proc Natl Acad Sci U S A.*
998 2017;114(40):E8372-E81.
999 44. Li Y, Renner DM, Comar CE, Whelan JN, Reyes HM, Cardenas-Diaz FL, et al.
1000 SARS-CoV-2 induces double-stranded RNA-mediated innate immune responses
1001 in respiratory epithelial-derived cells and cardiomyocytes. *Proc Natl Acad Sci U S*
1002 *A.* 2021;118(16).
1003 45. Sampaio NG, Chauveau L, Hertzog J, Bridgeman A, Fowler G, Moonen JP, et al.
1004 The RNA sensor MDA5 detects SARS-CoV-2 infection. *Sci Rep.*
1005 2021;11(1):13638.
1006 46. Shemesh M, Aktepe TE, Deerain JM, McAuley JL, Audsley MD, David CT, et al.
1007 SARS-CoV-2 suppresses IFNbeta production mediated by NSP1, 5, 6, 15, ORF6
1008 and ORF7b but does not suppress the effects of added interferon. *PLoS Pathog.*
1009 2021;17(8):e1009800.
1010 47. Lei X, Dong X, Ma R, Wang W, Xiao X, Tian Z, et al. Activation and evasion of type
1011 I interferon responses by SARS-CoV-2. *Nat Commun.* 2020;11(1):3810.
1012 48. Xia H, Cao Z, Xie X, Zhang X, Chen JY, Wang H, et al. Evasion of Type I Interferon
1013 by SARS-CoV-2. *Cell Rep.* 2020;33(1):108234.
1014 49. Uhlen M, Fagerberg L, Hallstrom BM, Lindskog C, Oksvold P, Mardinoglu A, et al.
1015 Proteomics. Tissue-based map of the human proteome. *Science.*
1016 2015;347(6220):1260419.
1017 50. Zhang Q, Bastard P, Liu Z, Le Pen J, Moncada-Velez M, Chen J, et al. Inborn
1018 errors of type I IFN immunity in patients with life-threatening COVID-19. *Science.*
1019 2020;370(6515).

51. Pruijssers AJ, George AS, Schafer A, Leist SR, Gralinksi LE, Dinnon KH, 3rd, et al. Remdesivir Inhibits SARS-CoV-2 in Human Lung Cells and Chimeric SARS-CoV Expressing the SARS-CoV-2 RNA Polymerase in Mice. *Cell Rep.* 2020;32(3):107940.

52. Bouhaddou M, Memon D, Meyer B, White KM, Rezelj VV, Correa Marrero M, et al. The Global Phosphorylation Landscape of SARS-CoV-2 Infection. *Cell.* 2020;182(3):685-712 e19.

53. Tohyama S, Hattori F, Sano M, Hishiki T, Nagahata Y, Matsuura T, et al. Distinct metabolic flow enables large-scale purification of mouse and human pluripotent stem cell-derived cardiomyocytes. *Cell Stem Cell.* 2013;12(1):127-37.

54. Howe KL, Achuthan P, Allen J, Allen J, Alvarez-Jarreta J, Amode MR, et al. Ensembl 2021. *Nucleic Acids Res.* 2021;49(D1):D884-D91.

55. Dobin A, Davis CA, Schlesinger F, Drenkow J, Zaleski C, Jha S, et al. STAR: ultrafast universal RNA-seq aligner. *Bioinformatics.* 2013;29(1):15-21.

56. Liao Y, Smyth GK, and Shi W. featureCounts: an efficient general purpose program for assigning sequence reads to genomic features. *Bioinformatics.* 2014;30(7):923-30.

57. Robinson MD, McCarthy DJ, and Smyth GK. edgeR: a Bioconductor package for differential expression analysis of digital gene expression data. *Bioinformatics.* 2010;26(1):139-40.

58. Zhou Y, Zhou B, Pache L, Chang M, Khodabakhshi AH, Tanaseichuk O, et al. Metascape provides a biologist-oriented resource for the analysis of systems-level datasets. *Nat Commun.* 2019;10(1):1523.

Figure Legends

Figure 1. SARS-CoV-2 infection of cardiac and lung AT2 cells is mediated by ACE2. (A) Schematic of cell differentiation and infection protocols. (B) Viral titres and genome copies in SARS-CoV-2 (VIC01) infected Vero, lung AT2 (H9) and cardiac (NKX2-5) culture supernatants. (C) Representative fluorescent confocal microscopy images of dsRNA (green) expression in VIC01 infected lung AT2 (SFTPC-positive) and cardiac (cTNT-positive) cells at 3 dpi. Titres in supernatants from cardiac and lung AT2 cells infected with VIC01 (WT) compared to cells infected with Alpha, Beta, Gamma and Delta variants (D) or Omicron (BA.1 and BA.2) variants (E).

Figure 2. SARS-CoV-2 entry and antiviral sensitivity is different between lung AT2 and cardiac cells. (A) Virus titer in supernatants from SARS-CoV-2 (VIC01) infected H9-derived WT and *ACE2* KO cardiac and lung AT2 cells. (B) Virus titer at 3 dpi in supernatants from lung AT2 (H9) and cardiac cells (NKX2-5) treated with two α-ACE2 antibodies or a human IgG1 isotype control before infection with SARS-CoV-2. (C) Virus titer at 3 dpi in supernatant from cardiac cells (red triangles) and lung AT2 cells (blue squares) infected with SARS-CoV-2 (VIC01) in the presence of Camostat, CA-074 or DMSO (vehicle control). Virus titres and genome copies at 3 dpi in supernatant from Vero, lung AT2 and cardiac cells infected with SARS-CoV-2 VIC01 in the presence of various concentrations of Remdesivir (D) or NHC (E).

Figure 3. Cardiac, but not lung AT2 cells, have a robust interferon signature following SARS-CoV-2 infection. (A) Principal Component Analysis (PCA) plot of uninfected (mock) and SARS-CoV-2 infected (virus) cardiac and lung AT2 cells at 1 and 3 dpi. (B) Venn diagram depicting the number of overlapping and unique differentially expressed genes compared to mock-infected. (C) Top representative WikiPathway (WP) terms of the enriched genes. Circle size is proportional to the number of genes that matched the pathway and color represents the LogP value as calculated by Metascape. (D) Heat map in Log2 fold change (FC) of representative interferon genes (compared to representative mock-infected samples at 1 dpi) separated by type as defined by WikiPathways. Columns on the right show the concordance between direction of fold change of RNAseq data and the LegendPlex/Taqman assays. For 1 dpi and 3 dpi, 3 lung samples and 2 cardiac samples were analyzed per group (mock, virus). (E) Cytokine concentrations in the supernatants of mock and SARS-CoV-2 infected cardiac and lung AT2 cells at 3 dpi.

Figure 4. SARS-CoV2 infection alters different signaling networks in heart and lung organoids. (A) Schematic of phosphoproteomics workflow. (B) Number of phosphorylated peptides, sites and proteins found in at 3 samples. (C) PCA plot of median-normalized phosphoproteome replicates from uninfected (mock) and SARS-CoV-2 infected (CoV) cardiac and lung AT2 cells at 18 and 24 hours post infection. Number of significantly (Padj < 0.05, FC >1.5) regulated phosphopeptides per timepoint (D) and their overlap (E) between cell types. Top 5 predicted drivers following SARS-CoV-2 infection in lung and cardiac cells (F) and in lung cells (G) at 72h post-infection. Adjusted

P-values (P.adj) are calculated based on the computation of Z-score probability distributions of a molecule to be a driver and adjusted using the Benjamini and Hochberg algorithm. (H) GO cellular components enriched in at least one condition ($P < 0.05$) that are related to endosomes. (I) Kinases with enriched substrates, which were selected for targeting. (J) Abundance of the PKC substrate MARCKS S170. (K) Abundance of the SRPK1 substrate SARS-CoV2 nucleocapsid protein S206.

Figure 5. Efficacy of kinase inhibitors against SARS-CoV-2 replication varies between Lung AT2 and cardiac cells. Cell viability (% relative to Vehicle control, black lines) and inhibition of SARS-CoV-2 growth (% relative to Vehicle control) in the presence of CDK (A), CHK (B), PKC (C) and, SRPK1 (D) inhibitors in lung AT2 cells (H9) and cardiac cells (NKX2-5) at 2 dpi. Dotted black lines indicate 50% virus inhibition or cell viability.

Figure S1. (A) Immunofluorescence images of lung culture from 3D organoids into 2D (AQP5, White; NKX2.1, Green; ACE2, Red). Heatmap analysis of lung-related (B) and cardiac-related (C) gene sets. (D) Viral titres and genome copies in supernatant from cardiac cells (ALK3-KO) infected with SARS-CoV-2 (VIC01). Viral genomes in supernatants from cardiac and lung AT2 cells infected with VIC01 (WT) compared to cells infected with Alpha, Beta, Gamma and Delta variants (E) or Omicron (BA.1 and BA.2) variants (F).

Figure S2. (A) PCR for *ACE2* in both the H9 and MCRIi010-A *ACE2* WT and KO clones. (B) Sanger sequencing of MCRIi010-A and H9 ACE2 KO clones. (C) ACE2 expression in ESCs/iPSCs and differentiated cardiac and lung AT2 cells. GAPDH was used as a loading control. (D) Relative expression of *ACE2* in the H9 ACE2 KO-derived cardiac and lung AT2 cells compared to lung AT2 WT. (E) Representative flow cytometry plot of proteins associated with pluripotency (CD9, EPCAM, SSEA4) in the H9 *ACE2* KO line. (F) Representative flow cytometry plot of cardiac proteins (c-TnT, α-actinin) following differentiation in H9 WT and ACE2 KO lines. (G) Virus titer in supernatant from SARS-CoV-2 infected ACE2 KO and WT MCRIi010-A-derived cardiac cells. (H) Representative fluorescent confocal microscopy images of ACE2 (red) and dsRNA (green) expression in WT and *ACE2 KO* cardiac (cTNT-positive) and lung AT2 (SFTPC-positive) cells (H9 and MCRIi010-A). Scale bars are highlighted on each panel.

Figure S3. (A) Heat map in log2 counts per million (CPM) representing the gene expression of ACE2, TMPRSS2 and Cathepsin L (CTSL) in uninfected and SARS-CoV-2-infected iPSC-derived lung AT2 and cardiac cells at 1 and 3 dpi. (B) Relative expression of ACE2, TMPRSS2 and Cathepsin L in iPSC-derived cardiac and lung AT2 ACE2 KO cells compared to lung AT2 WT. (C) Viral genome copies in supernatants from cardiac (red triangles) and lung AT2 (blue squares) cells at 3 dpi infected with SARS-CoV-2 in the presence of Camostat, CA-074 Me or DMSO.

Figure S4. (A) Cell viability in uninfected Vero, lung AT2 and cardiac cells following 3 days culture in the presence of Remdesivir or NHC at the indicated concentrations. (B)

Virus titer and viral genome copies in the supernatant at 3 dpi in Vero, lung AT2, NKX2-5 cardiac and ALP3K KO cells infected with SARS-CoV-2 in the presence of 1μM or 10μM Favipiravir, Chloroquine, Tizoxanide or Piperaquine. Cell viability of uninfected cells after 3 days culture in the presence of the above drugs.

Figure S5. (A) Extended heat map in Log2 fold change (FC) of representative interferon genes (compared to representative mock-infected samples at 1 dpi) separated by type as defined by WikiPathways. (B) Extended Plot of top enriched WP terms. (C) Relative expression of IFN pathway genes compared to mock-infected cells. (D) Gene network diagram of the GO Term 'response to interferon gamma' (GO:0034341). Node colors are log2 fold change of the gene in the respective tissue type.

Figure S6. (A) All GO cellular components enriched in at least one condition ($P < 0.05$). (B) All kinases with reported substrates enriched in at least one condition ($P < 0.05$).

Figure S7. Cell viability (% relative to Vehicle control, black lines) and inhibition of SARS-CoV-2 growth (% relative to Vehicle control) in the presence of indicated compounds in H9 cardiac cells (A), H9 lung AT2 cells (B) and NKX2-5 cardiac (C) cells at 3 dpi.

Table S1. List of sites phosphorylated on SARS-CoV-2 proteins in infected cardiac and lung cells

Protein	Phosphorylation Site	Lung	Cardiac
ORF1a	S2644	+	+
Spike	S1261	+	+
Membrane	S213	+	+
Membrane	S214	+	+
Membrane	T208	-	+
Membrane	S212	-	+
Nucleocapsid	S2	+	+
Nucleocapsid	S21	+	+
Nucleocapsid	S23	+	+
Nucleocapsid	T24	+	+
Nucleocapsid	S26	+	+
Nucleocapsid	T76	-	-
Nucleocapsid	T79	+	+
Nucleocapsid	T166	+	+
Nucleocapsid	Y172	+	-
Nucleocapsid	S176	+	+
Nucleocapsid	S180	+	+
Nucleocapsid	S183	-	-
Nucleocapsid	S184	+	+
Nucleocapsid	S186	-	-
Nucleocapsid	S188	-	-
Nucleocapsid	S194	+	+
Nucleocapsid	S197	+	+
Nucleocapsid	T198	+	+
Nucleocapsid	S201	+	+
Nucleocapsid	S202	+	+
Nucleocapsid	T205	+	+
Nucleocapsid	S206	+	+
Nucleocapsid	T245	+	+
Nucleocapsid	T379	+	+
Nucleocapsid	T391	+	+
Nucleocapsid	T393	+	+
Nucleocapsid	S404	+	+
Nucleocapsid	S412	+	+
Nucleocapsid	S416	+	+
ORF9b	S50	+	+

Table S2. Compounds for antiviral testing from MedChemExpress

Compound	Target Kinase(s)	Catalogue
Abemaciclib	CDK4 and CDK6	HY-16297A
Alectinib (CH5424802)	SRPK1	HY-13011
AZD1080	GSK-3	HY-13862
Bisindolylmaleimide I	PKC	HY-13867
CCT241533 hydrochloride	CHK2	HY-14715B
CCT251545	CDK8, CDK19 and WNT	HY-12681
Dinaciclib	CDK2, CDK5, CDK1, and CDK9	HY-10492
Flavopiradol	CDK1, CDK2, CDK4	HY-10005
GW788388	ALK5 and TGF-β type II receptor	HY-10326
Palbociclib hydrochloride	CDK and CDK6	HY-50767A
R-10015	LIMK	HY-120097
R406 free base	Syk/FLT3	HY-11108
Samuraciclib hydrochloride hydrate	CDK7	HY-103712B
SNS-032	CDK2, CDK7, and CDK9	HY-10008
SPHINX31	SRPK1	HY-117661
Trilaciclib hydrochloride	CDK4 and CDK6	HY-101467A

ALK5: Activin-like kinase 5, CDK: Cyclin dependent kinase, CHK: Checkpoint, FLT3: FMS-like tyrosine kinase 3, GSK-3: Glycogen synthase kinase 3, LIMK: LIMK domain kinase, PKC: Protein kinase C, SRPK1: Serine/arginine-rich protein-specific kinase, TGF-β: Transforming growth factor beta.

Table S3. TaqMan Probes for qPCR

Gene	Target Kinase(s)
GAPDH	Hs02758991_g1, Hs02786624_g1
TMPRSS2	Hs00237175_m1
ACE2	Hs01085333_m1
CTSL	Hs00964650_m1
EIF4E	Hs00854166_g1
IFN-β1	Hs01077958_s1
IL-6	Hs00174131_m1
IRF9	Hs00196051_m1
IRS1	Hs00178563_m1
STAT1	Hs01013996_m1
STAT1	Hs01013116_g1
IRS2	Hs00275843_s1
PRKCD	Hs01090047_m1
SOCS1	Hs00705164_s1
REL	Hs00968440_m1
MAP2K6	Hs00992389_m1
IFITM3	Hs03057129_s1
OAS2	Hs00942643_m1

Figure 1.

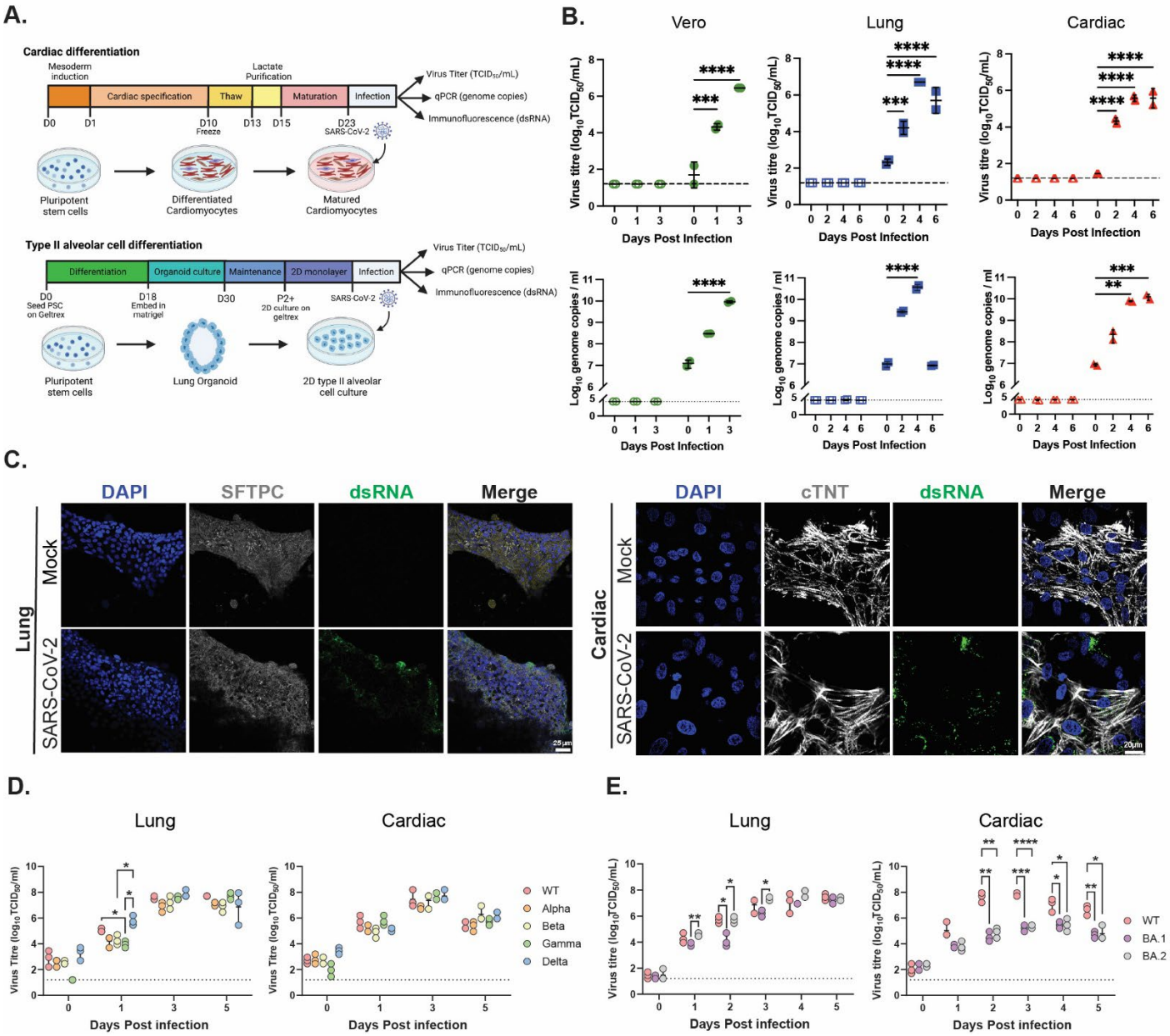

Figure 2.

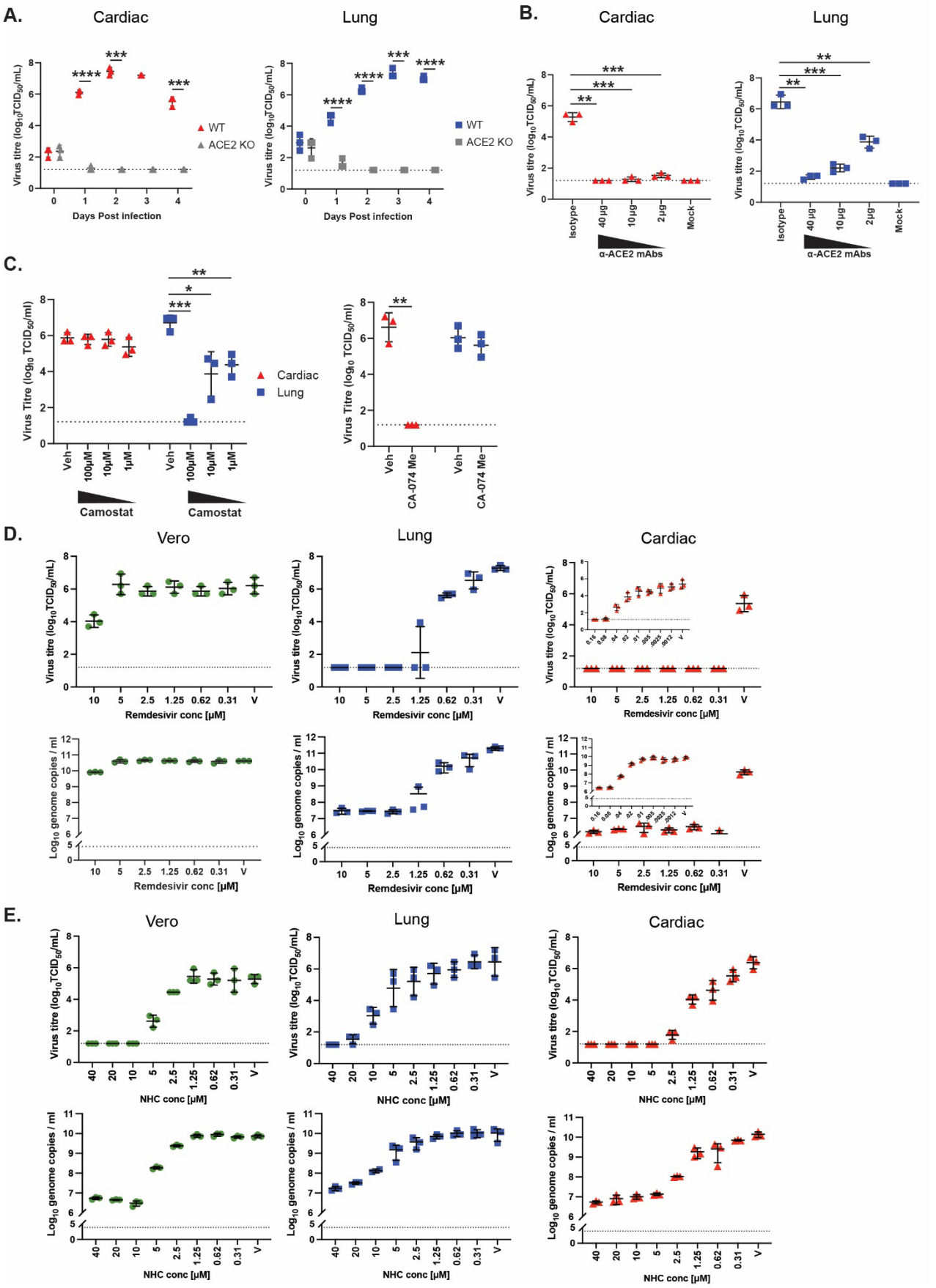

Figure 3.

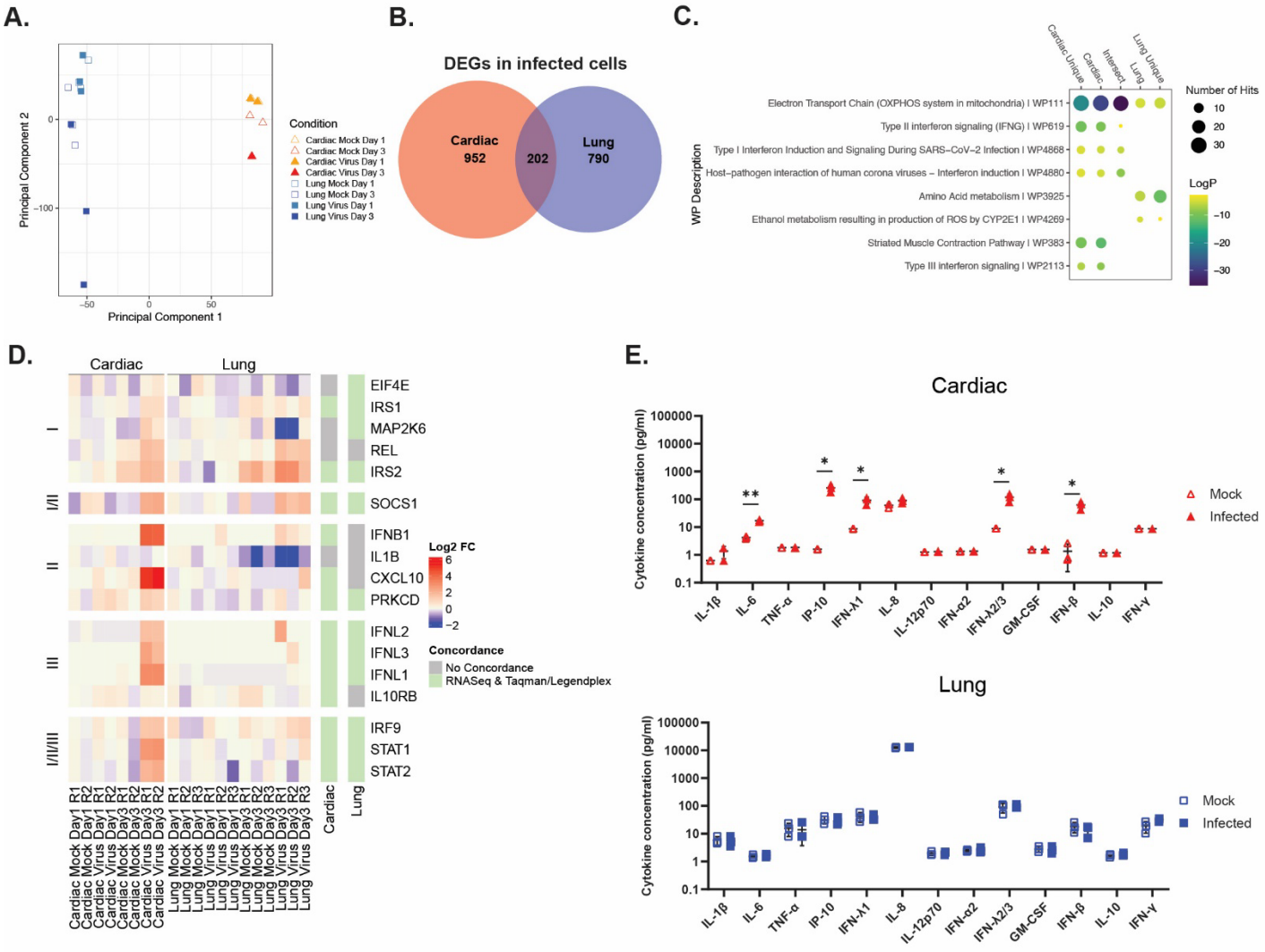

Figure 4.

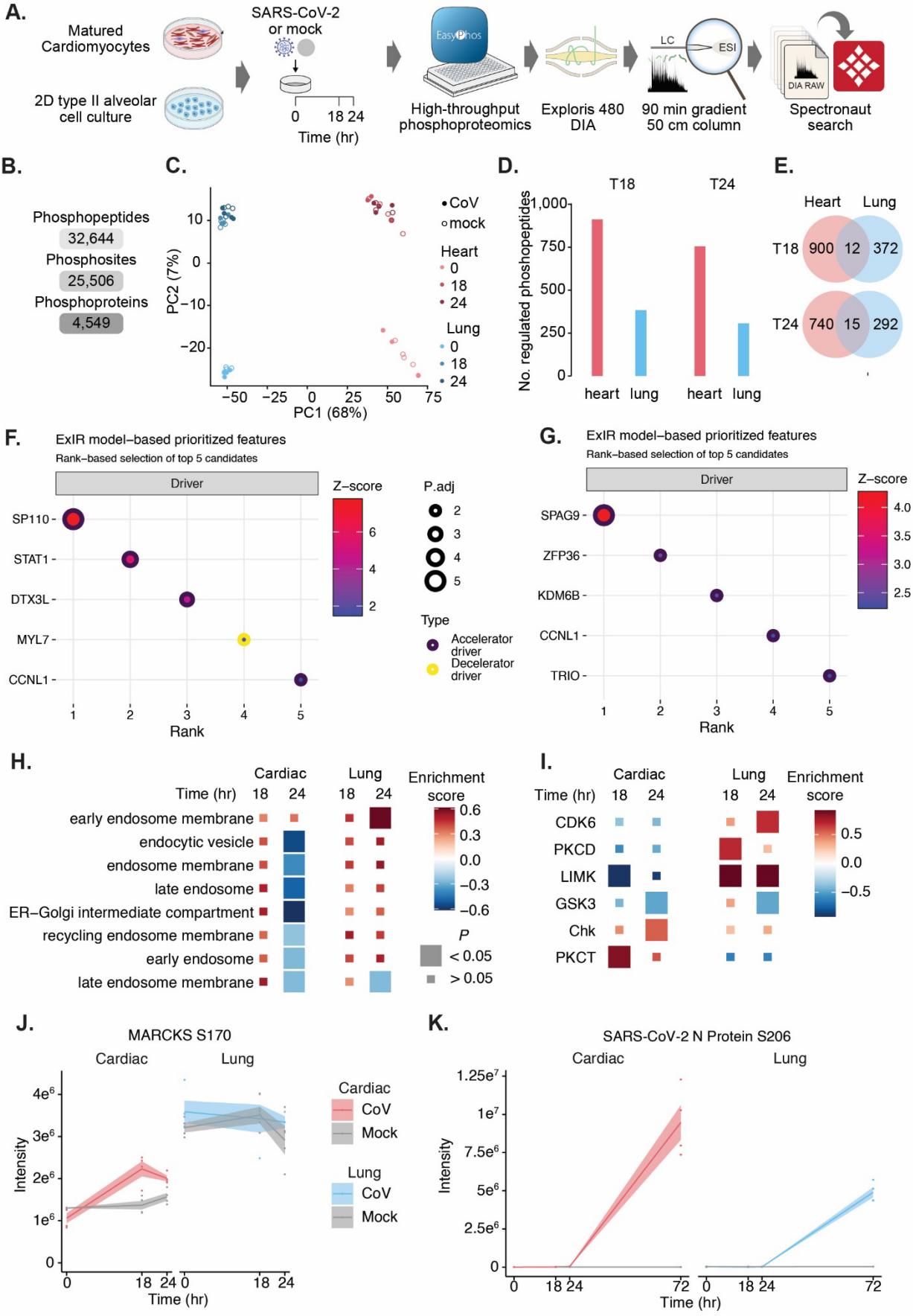

Figure 5.

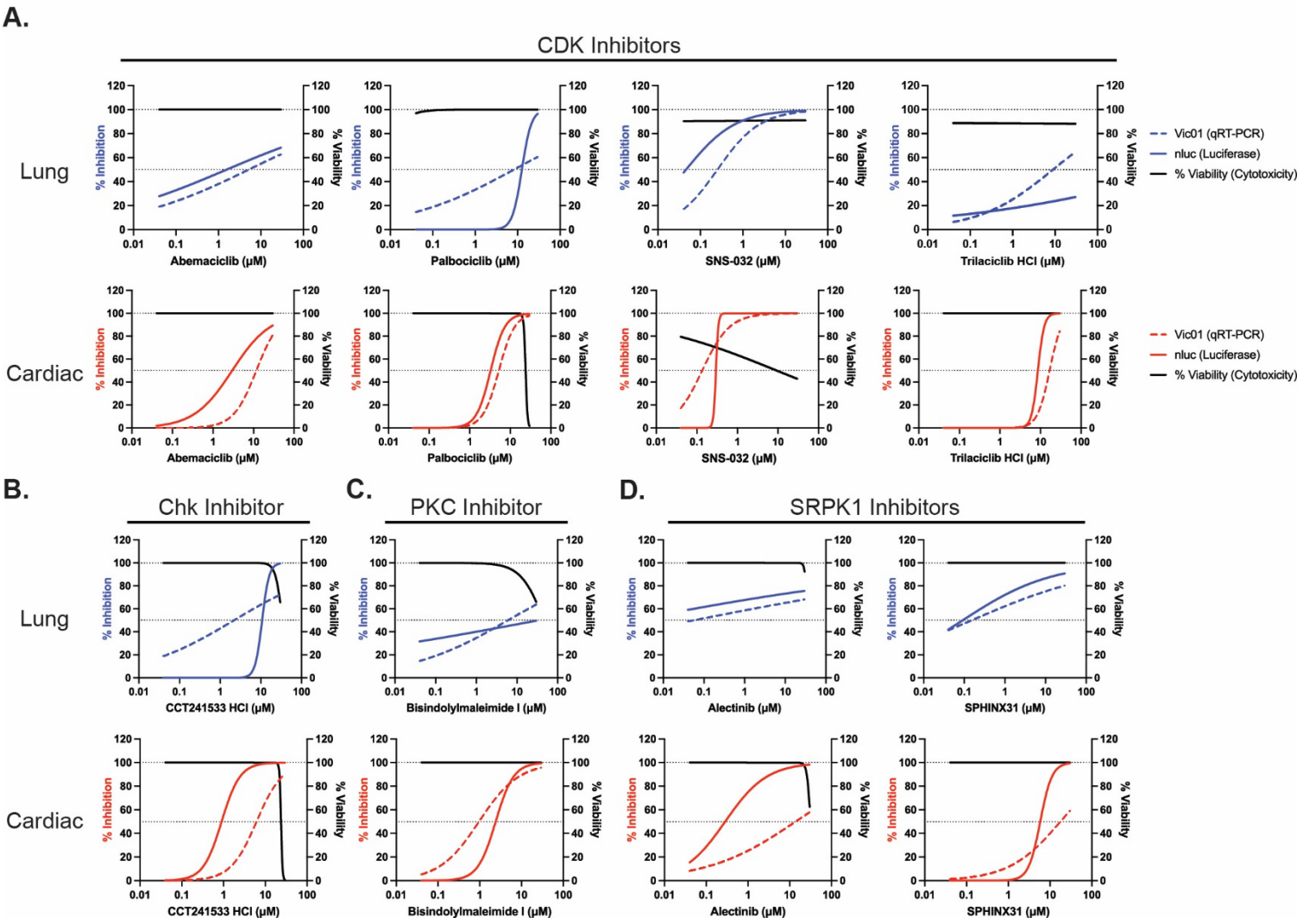

Figure S1

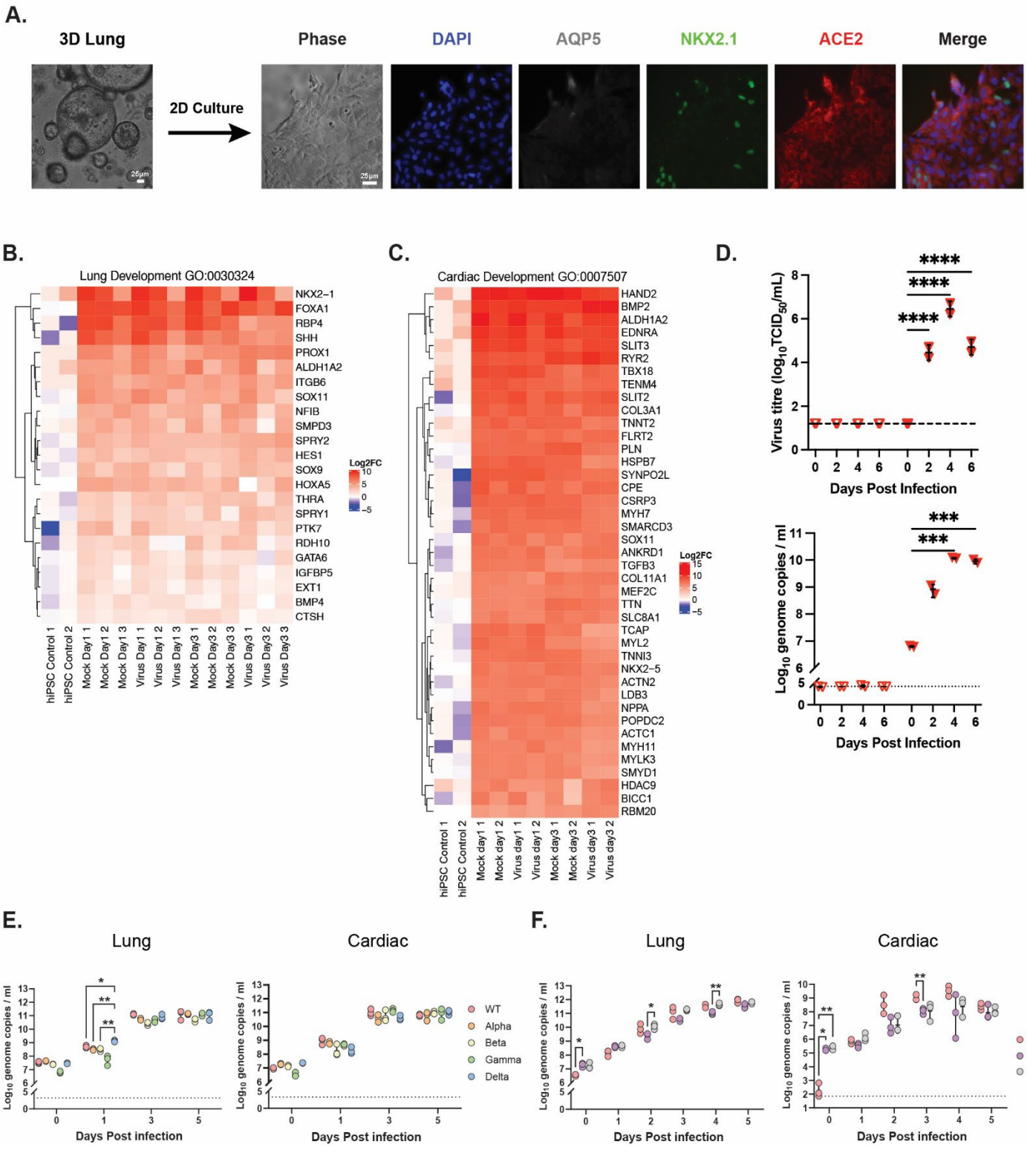

Figure S2

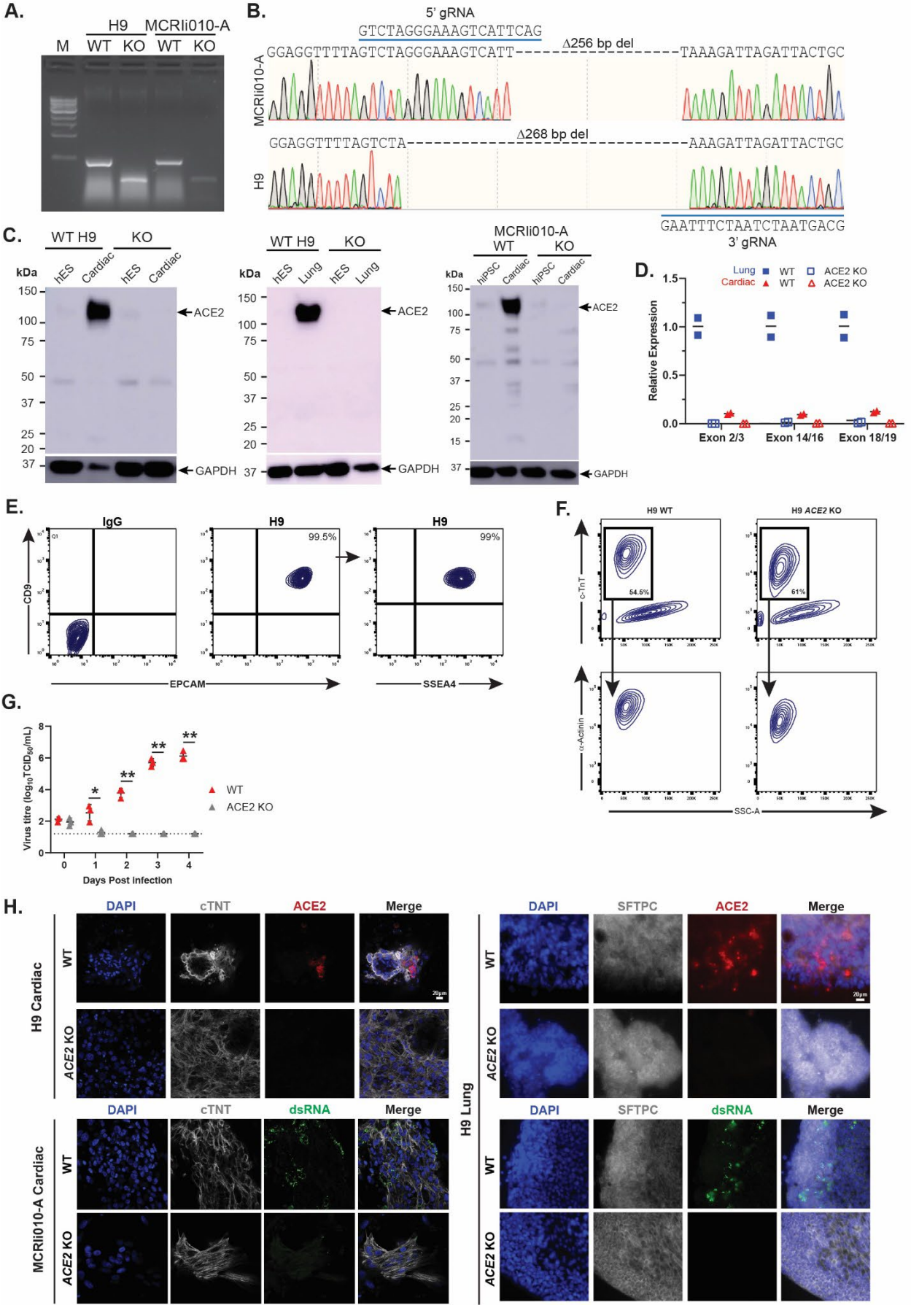

Figure S3

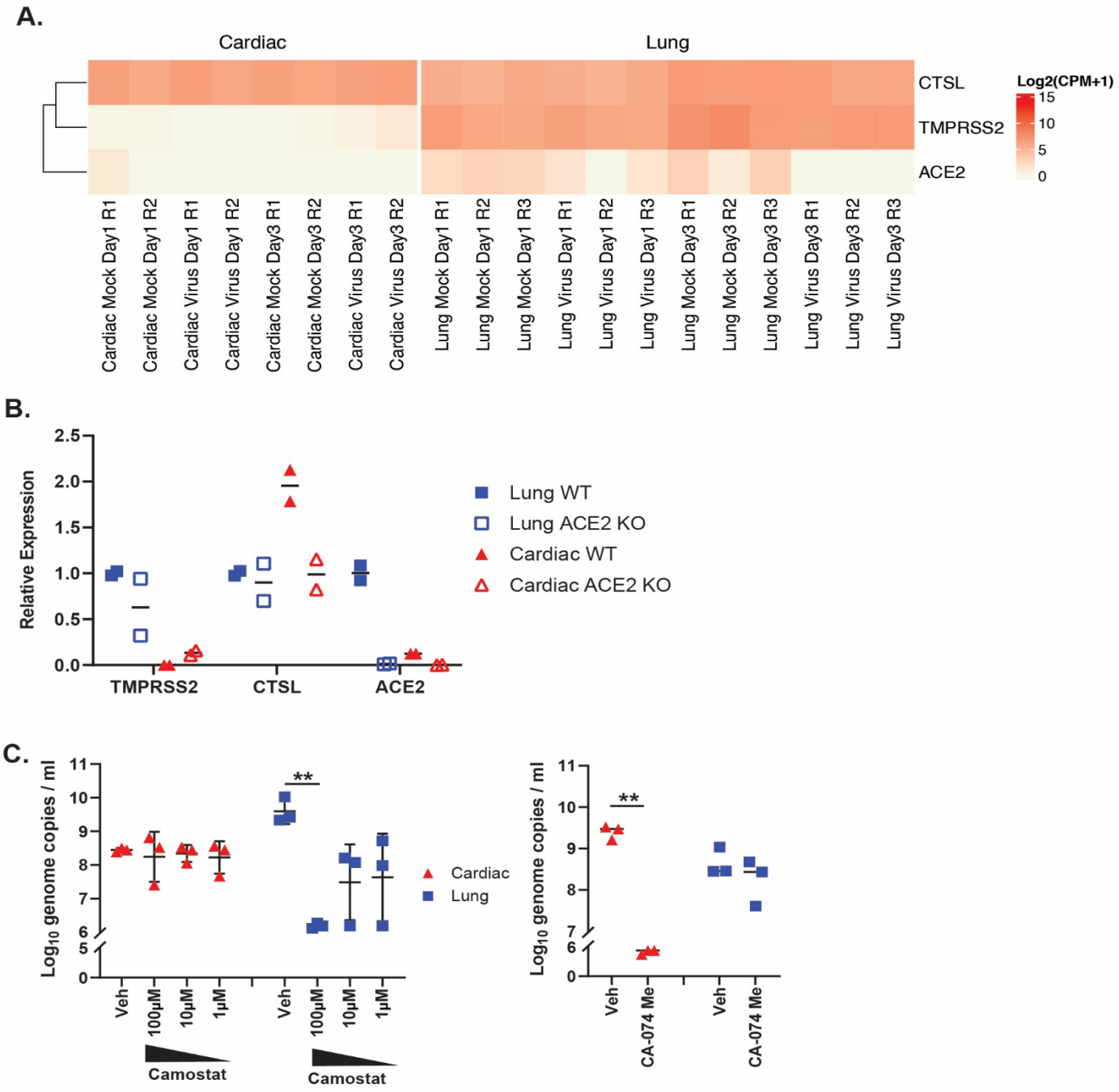

Figure S4

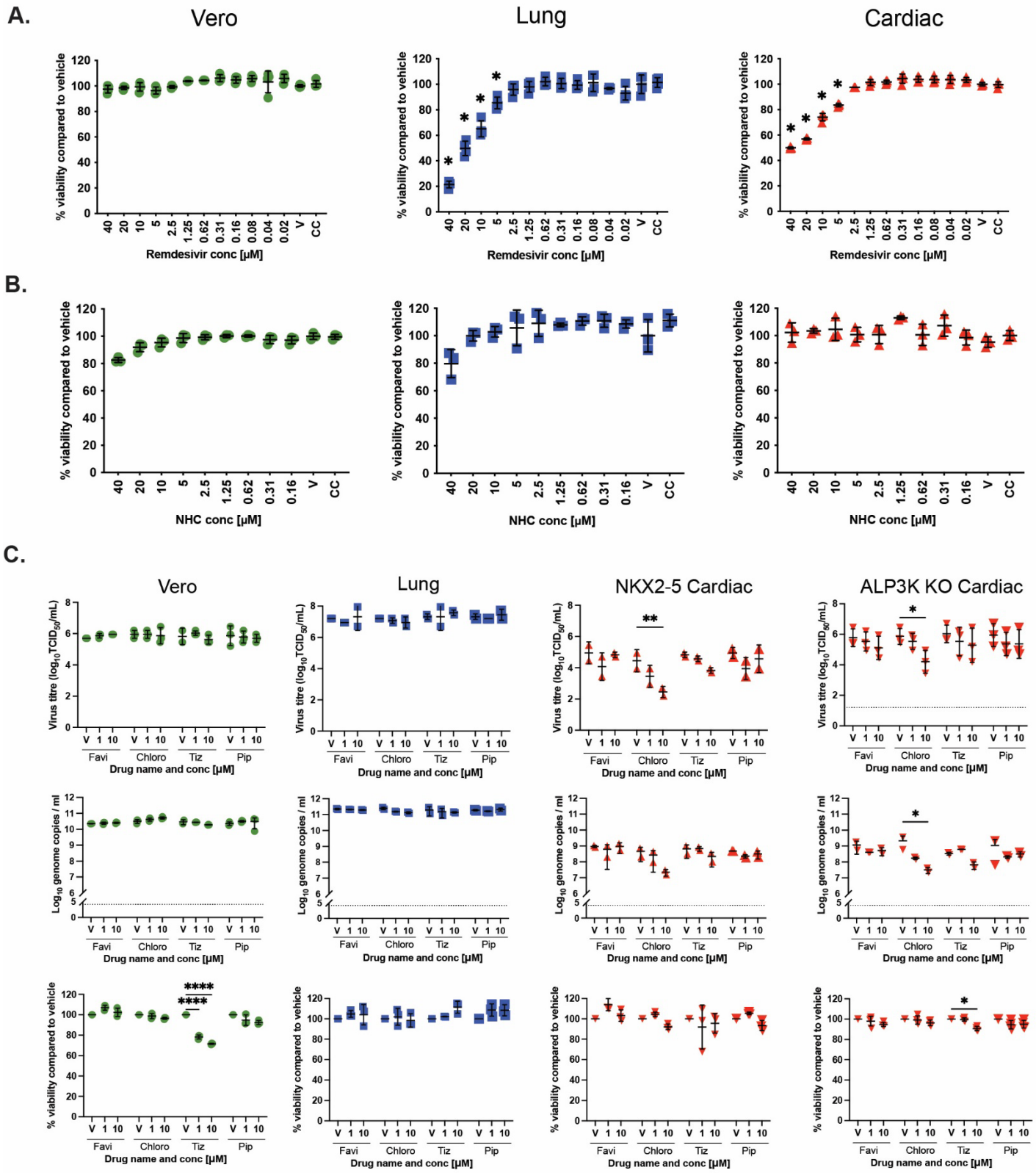

Figure S5

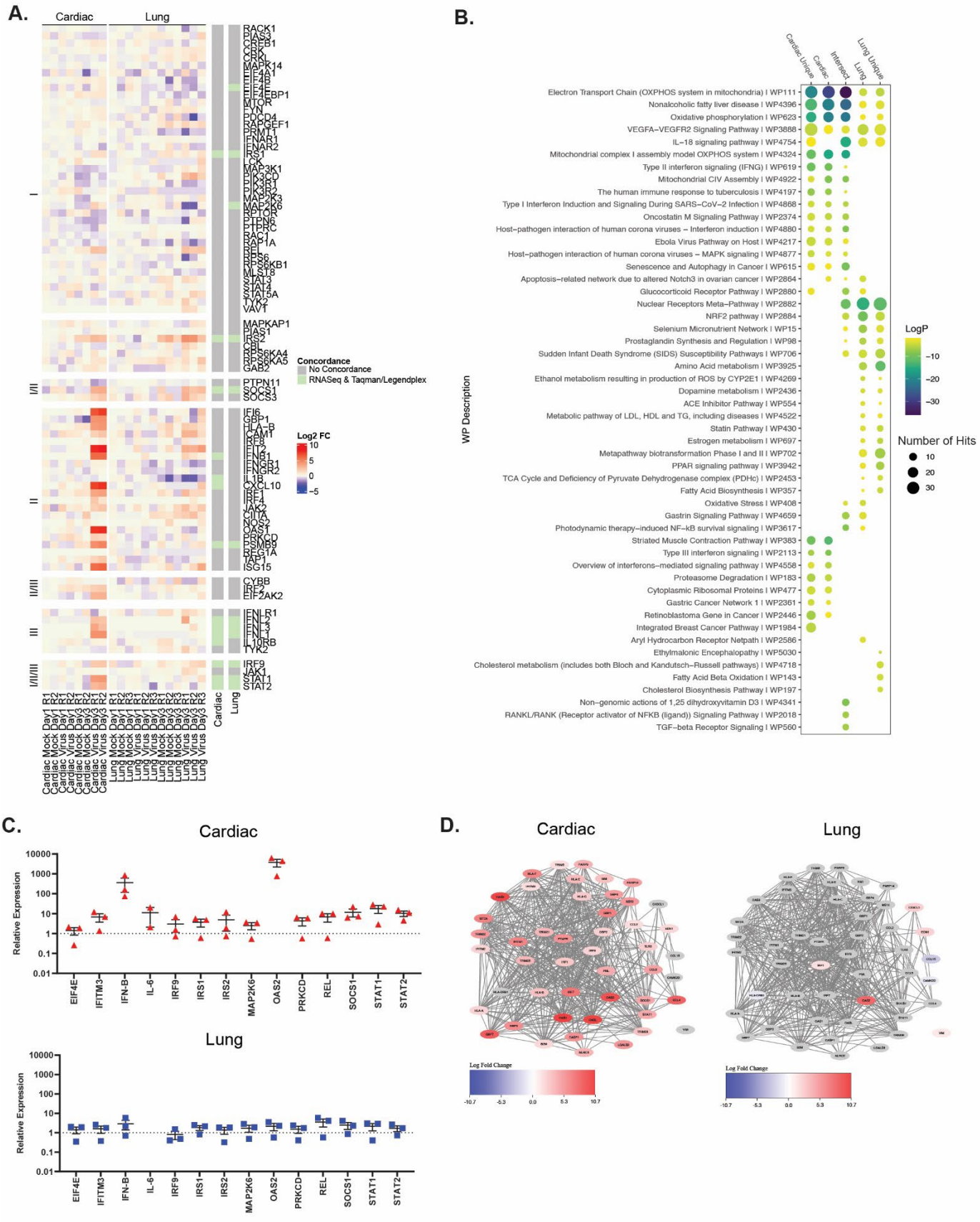

Figure S6

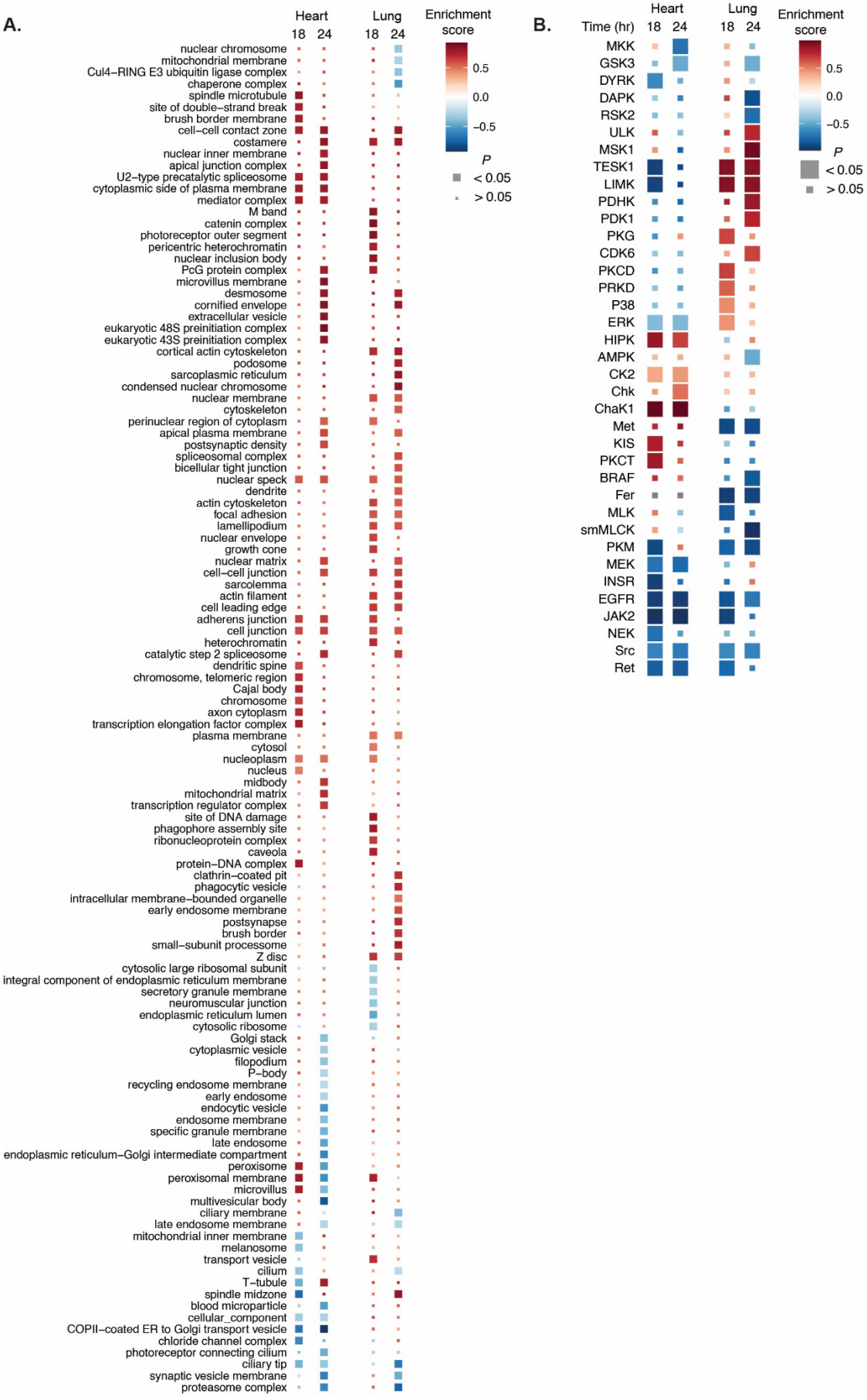

Figure S7